The M6.0 24 August 2014 South Napa Earthquake

Thomas M. Brocher[1], Annemarie S. Baltay[1], Jeanne L. Hardebeck[1], Fred F. Pollitz[1], Jessica R. Murray[1], Andrea L. Llenos[1], David P. Schwartz[1], James Luke Blair[1], Daniel J. Ponti[1], James J. Lienkaemper[1], Victoria E. Langenheim[2], Timothy E. Dawson[3], Kenneth W. Hudnut[4], David R. Shelly[5], Douglas Dreger[6], John Boatwright[1], Brad T. Aagaard[1], David J. Wald[7], Richard M. Allen[6], William D. Barnhart[7,8], Keith L. Knudsen[1], Benjamin A. Brooks[1], Katherine M. Scharer[4]

[1]U.S. Geological Survey, MS 977, 345 Middlefield Road, Menlo Park, CA 94025

[2]U.S. Geological Survey, MS 989, 345 Middlefield Road, Menlo Park, CA 94025

[3]California Geological Survey, 345 Middlefield Road, Menlo Park, CA 94025

[4]U.S. Geological Survey, 525 South Wilson Ave., Pasadena, CA 91106

[5]U.S. Geological Survey, MS 910, 345 Middlefield Road, Menlo Park, CA 94025

[6]Seismo Lab, 215 McCone Hall #4760, UC Berkeley, Berkeley, CA 94720

[7]U.S. Geological Survey, 1711 Illinois Ave., Golden, CO 80401

[8]Department of Earth and Environmental Sciences, University of Iowa, Iowa City, IA 52242

Introduction

The M6.0 South Napa earthquake at 10:20 GMT 24 August 2014 was the largest earthquake to strike the greater San Francisco Bay Area since the M6.9 1989 Loma

Prieta earthquake. The rupture from this right-lateral earthquake propagated mostly unilaterally to the north and updip, directing the strongest shaking towards the city of Napa, where peak ground accelerations between 45% g and 61% g were recorded and MMI intensities of VII-VIII were reported. Tectonic surface rupture with dextral slip of up to 46 cm was observed on a 12.5-km-long segment, some of which was along a previously mapped strand of the West Napa Fault system, although the rupture extended to the north of the mapped Quaternary strand. Modeling of seismic and geodetic data suggest an average coseismic slip of 50 cm with a maximum slip of about 1 m at depths of 10 to 11 km. We observed up to 35 cm of afterslip along the surface trace in the week following the mainshock, primarily along the southern half of the surface rupture that experienced relatively little coseismic offset. Relocation of the sparse aftershock sequence suggests en-echelon SW and NE dipping fault planes, reflective of the complex fault geometry in this region. The Napa Basin and historic and late Holocene alluvial flood deposits in downtown Napa amplified the ground motions there. Few ground failures were mapped, reflecting the dry season as well as a persistent drought which had lowered the ground water table, and the short duration of strong shaking in the epicentral area.

Tectonic Setting of the South Napa Earthquake

The South Napa fault rupture lies within an 80-km-wide set of major NNW trending

faults of the San Andreas Fault system forming the boundary between the Pacific and North American tectonic plates (Jennings, 1994; Figure 1). The West Napa Fault system is a relatively minor strike-slip fault in the Contra Costa shear zone, which transfers slip between the Northern Calaveras, West Napa, and Concord Faults (Unruh and Kelson, 2002a, b; Kelson and others, 2004, 2005; Wesling and Hanson, 2008; Brossy et al., 2010). Block modeling of GPS data estimated a slip rate of 4.0 ± 3.0 mm/year on the West Napa fault (D'Alessio et al., 2005). In the Uniform California Earthquake Rupture Forecast model the entire Contra Costa shear zone was assigned a maximum slip rate of 1 mm/year (Field et al., Appendix C, page 18, 2013). The earthquake was located near the eastern shore of San Pablo Bay midway between two major active fault systems: the Hayward-Rodgers Creek Fault system 12 km to the west and the Concord-Green Valley Fault system 13 km to the east. The earthquake epicenter lies 1.7 km west of the main mapped surface trace of the West Napa Fault system, and close to the surface traces of the lesser known Carneros and Franklin Faults (Graymer et al., 2002). Although several faults are mapped in the vicinity of the earthquake, only the West Napa Fault system is known to have displaced Holocene-age sediments (Wesling and Hanson, 2008).

The West Napa Fault system forms the western margin of a basin that underlies much of Napa Valley. The basin, filled with Cenozoic sedimentary and volcanic deposits, is approximately 2 km deep beneath the city of Napa. The South Napa earthquake occurred where the prominent east-facing gravity and magnetic gradients associated with the main bedrock strand of the West Napa Fault system diminish and are replaced

by prominent west-facing gravity gradients that mark the eastern margin of the San Pablo Bay basin and the Carneros and Franklin Faults (Langenheim et al., 2006). The 2000 M4.9 Yountville earthquake was attributed to the main bedrock strand of the West Napa Fault system 20 km north-northwest of the South Napa epicenter (Langenheim et al., 2006). Modeling of potential-field data, coupled with aftershock locations, indicates a steep southwest dip for the main bedrock strand at this location.

Historically, the M7.8 1906 San Andreas Fault earthquake and the M6.3 1898 Mare Island earthquake both caused shaking in this region sufficient to seriously damage structures at Mare Island. The 1898 earthquake may have occurred about 20 km to the northwest of Mare Island on the southern Rodgers Creek Fault (Toppozada et al., 1981; Bakun, 1999), although analysis after the South Napa earthquake locates that earthquake closer to Mare Island (Hough, 2014). Although the 2000 M4.9 Yountville earthquake ruptured the West Napa Fault north of Napa, its energy was directed south towards Napa, where it produced damage.

ShakeAlert EEW Performance

The prototype earthquake early warning (EEW) system, developed by the U.S. Geological Survey, University of California Berkeley, Caltech, Eidgenössische Technische Hochschule **(**ETH), and the University of Washington, named ShakeAlert (Given et al.,

2014), successfully delivered an alert for the earthquake. The first ShakeAlert (based on ElarmS) used data from four stations, had an estimated magnitude of 5.7, and was issued 5.1 seconds after the earthquake originated. The locations and magnitudes of the earthquake provided by ShakeAlert were stable and remained accurate as an ever-increasing number of stations were included in the real-time analysis. The sending of the alert at 5.1 seconds after origin time provided prototype ShakeAlert users in Berkeley and San Francisco about 10 seconds of warning prior to the onset of the strongest shaking at those locations (intensity IV). With the available network geometry and communications, the "blind zone" of the ElarmS alert had a radius of about 16 km. The four stations that contributed to the first ElarmS alert all provided 1 second data packets, but the latency in transmitting data to the processing center ranged from 0.27 seconds to 2.62 seconds. A denser seismic network and/or decreasing the latency in transmitting data to less than a second would have allowed alerts to be issued in less than 3 seconds for this event, reducing the blind zone to a radius of about 8 km, allowing an alert much closer to the epicenter. The first EEW alert based on the onsite algorithm was issued 10.9 seconds after the earthquake origin time.

Near-Real Time Earthquake Information Products

The first location, magnitude, focal mechanism, and ShakeMap, a map showing the shaking intensity (Wald, 2012), were reported 4 minutes after the origin time of the

earthquake. The first ShakeCast, based on the ShakeMap and user defined estimates of infrastructure fragility (Wald, 2012), was prepared for the California Department of Transportation 11 minutes after the earthquake. The first PAGER alert of probable fatalities and economic loss based on population exposure to the shaking (Wald, 2012) was produced 13 minutes after the origin time. As the ShakeMap was updated as additional strong motion recordings were retrieved and incorporated, the PAGER alert changed from Yellow to Orange to Red based on projected direct economic losses, which are reported to be on the order of one-half billion dollars (EERI, 2014). All versions of PAGER estimated between 0 and 10 fatalities; one fatality was reported. These products are available at the USGS Event Summary page for this earthquake (see data availability section). As for the ShakeAlert, increased network density and/or faster data data telemetry would have improved system performance.

The earthquake was widely felt in the San Francisco Bay Area. The Did You Feel It? (DYFI) community intensity website received more than 41,000 entries, with the highest reported intensities of VIII in Napa. The earthquake was reported as felt by more than one respondent 300 km to the east in Reno, Nevada, 340 km to the north in McKinleyville, California, and 440 km south in Bakersfield, California. Geocoded DYFI entries show that the highest intensities were reported north of the epicenter consistent with directivity estimates for the earthquake, although intensities of VII were also reported in northern Vallejo. Because the internet service to the most heavily

impacted areas was down for an extended time, few DYFI reports were received from within the City of Napa.

California Earthquake Clearinghouse

Within twelve hours of the mainshock, and for the first time since the 1994 Northridge earthquake, the California Earthquake Clearinghouse opened a physical clearinghouse in a Caltrans facility located in Napa (EERI, 2014). The Clearinghouse is a cooperative organization in which any agency interested in post-earthquake information is welcome to participate. In addition to the California Geological Survey that serves as the permanent lead coordinating agency, the founding and managing partners of the Clearinghouse include the California Office of Emergency Services, the California Seismic Safety Commission, the Earthquake Engineering Research Institute, and the U.S. Geological Survey. The California Department of Transportation, Caltrans, also provided a communications van that supported high-speed internet connections. The Clearinghouse, which included GIS staff, provided logistics support to the field crews, assisted in obtaining overflights of the surface rupture, and served to coordinate the field surveys being made of the surface rupture and ground deformation. Morning and evening meetings were held to debrief the field crews. The Clearinghouse closed in the evening of 26 August.

Mainshock Location, Magnitude, Focal Mechanism, and Finite Fault Inversion

Initial estimates of the hypocenter of the Mw6.0 (with a moment of 1.33 x 10^{18} N-m) earthquake, which occurred on 24 August 2014, at 10:20:44 UTC (3:20:44 local time), placed it about 8 km south-southwest of Napa at a depth of 11.3 ± 0.2 km. Although the relative depths have uncertainties of a few hundred meters, the absolute depth uncertainties could be on the order of a few kms due to velocity model uncertainties. [Relocation of the event (described below) yield an revised depth of 9.4 km.] 146 stations and 161 phases with an azimuthal gap of 29° were used to locate the hypocenter. The distance to the nearest station was 4.0 km (Figure 1), resulting in locations having reasonable depth control for the mainshock and its aftershocks.

Focal mechanisms are consistent with right-lateral motion along a plane striking 165°, dipping 85° to the SW. This plane is compatible with the observed tectonic surface rupture. Moment tensor solutions by UC Berkeley also show right lateral motion along a plane having nearly an identical strike, 157° or 158°, with a rake of 172°.

A preliminary slip model for the earthquake, based on seismic data, shows that the rupture propagated mostly north-northwest and updip (Figure 2). Slips at depth averaged about 50 cm in the elongated slip patch with a maximum of about one meter

at depths of 10 to 11 km. This northward rupture propagation would have directed seismic energy toward Napa and produced the intensity distribution reported by DYFI.

Coulomb stress transfer models calculated for the earthquake using *Coulomb 3.4* (www.coulombstress.org) were consistent with a clear seismicity rate increase north of the mainshock, and a modest increase south of the mainshock, roughly along the West Napa fault, where the stress is calculated to have increased by ~0.5 bars (Parsons et al., 2014). Other small earthquakes occurred on or near the Green Valley fault where the Coulomb stress is calculated to have increased by ~0.25 bars, although this section of the Green Valley fault is very active as recorded instrumentally. Coulomb stress changes of >0.5 bars are often but not always associated with increases in the rate of earthquakes, whereas changes of <0.1 bars are probably not important for triggering aftershocks.

Aftershock Sequence and Location

The aftershock sequence after one month (80 M ≥ 1.8 aftershocks) was nearly 4 times less productive than for the 2004 M6 Parkfield earthquake (320 M ≥ 1.8 aftershocks). Both M6 earthquakes, however, have *b*-values in the 0.7-0.8 range, similar to other Northern California M~6 aftershock sequences. Moreover, despite the relatively low aftershock productivity, the sequence is well described by epidemic-type aftershock

sequence models (Ogata, 1988). The largest aftershock to date, a M3.9 event, occurred just over 2 days after the mainshock. This aftershock was among the first to rupture south of the mainshock and triggered a cluster of its own aftershocks on the southern end of the West Napa Fault (Figure 1).

The first week of aftershocks were relocated using the *tomoDD* code (*Zhang and Thurber*, 2003), and the 3D seismic velocity model and station corrections of *Hardebeck et al.* (2007). Catalog P-wave and S-wave arrival times were used for relocation, as well as relative arrival times from waveform cross-correlation. A matched filter approach was applied to identify aftershocks that do not appear in the network catalog.

We relocated all catalog earthquakes, and all matched-filter-detected events with at least 8 waveform differential times with correlation coefficient ≥0.8. We performed 20 iterations of *tomoDD*, the first 10 with the catalog times given more weight, and the last 10 with the waveform differential times given more weight. The relocated catalog consists of 375 hypocenters: 147 catalog aftershocks, 227 aftershocks detected by the matched filter approach, and the mainshock hypocenter. The relocated depth of the mainshock hypocenter is 9.4 km.

Although the surface rupture of the mainshock was well expressed, the fault plane of the mainshock is not well defined by the aftershocks. Most of the aftershocks occur between 8 and 11 km depth, and form a diffuse ~10-km-long NNW-trending feature to

the NNW of the mainshock hypocenter (Figure 3). In cross-section, a sharply-defined NE-dipping seismicity plane is apparent north of the hypocenter, implying significant geometric complexity. In addition to the main aftershock zone, there are a few clusters of aftershocks to the northwest, close to but south-southeast of the Yountville earthquake and its aftershocks, a cluster of aftershocks to the south of the mainshock, and a cluster of earthquakes in the Green Valley fault zone that is ~30 km directly to the east of the main aftershock zone.

To better understand the complex geometry of the aftershocks, the Optimal Anisotropic Dynamic Clustering (OADC) algorithm (*Ouillon et al*., 2008) was used to identify the simplest planar fault geometry that fits the events of the main aftershock zone. Aftershock locations were fit to within the uncertainty, assumed here to be 0.5 km for all events. To account for sensitivity to randomness in the OADC procedure, we ran OADC 3000 times, and use the suite of results to identify stable features and their uncertainty. The OADC algorithm returns two stable planes, which occur in 84% and 73% of the runs. No other plane occurs in more than 30% of the runs.

One of the OADC-determined planes corresponds to the NE-dipping seismicity structure visible in cross-section. This plane strikes 357 ± 25° and dips 33 ± 24° to the east. The other plane strikes 162 ± 9° and dips 72 ± 19° to the SW. This structure is visible only as a diffuse zone of seismicity in some cross-sections. This second plane is similar in orientation to the fault plane of the mainshock moment tensor, so it may represent

aftershocks occurring in the area around the mainshock rupture. The occurrence of most aftershocks to the west of the mapped surface rupture is consistent with the SW dip of the mainshock fault plane.

The mainshock hypocenter and many of the aftershocks occur near the intersection of the two apparent fault planes. The plane intersection deepens to the SSE, due to the difference in strike, corresponding to a slight deepening of the densest aftershock zone towards the SSE. The aftershock geometry suggests that stress is concentrated at the intersection of two active fault structures, encouraging nucleation of the mainshock and the majority of aftershocks. If this model is applied more broadly, it suggests that seismicity streaks reflect the linear intersection of planar faults. In previous earthquakes, seismicity streaks can persist over decades at least, and are not reset by stress redistribution when a mainshock occurs (*e.g. Thurber et al*., 2006), also suggesting a link to fault geometry.

Spatial Variability of Strong Ground Motions

Peak ground accelerations (PGA) of 45 to 61% g and peak ground velocities (PGV) of 45 to 90 cm/s from the M6.0 South Napa earthquake were recorded in the Napa area, damaging many older buildings and resulting in more than 100 red-tagged structures (Boatwright et al., this volume). The recorded data are of engineering interest as nine

strong motion recordings were in excess of 30% g, three strong motion recordings were made at epicentral distances less than 10 km, and 20 recordings were made at epicentral distances less than 20 km. The highest peak ground acceleration (0.995% g) was recorded at Crockett beneath the Carquinez Bridge: it is possible that the acceleration recorded there reflects soil-structure interaction or an unusual path effect.

The recorded ground motions for PGA, PGV and spectral accelerations (PSA) at periods of 0.3 s, 1.0 s and 3.0 s were compared to five ground motion prediction equations (GMPEs): the four NGA-West2 GMPEs as well as that of Graizer and Kalkan (2015), to analyze both relative source and attenuation properties (see also Baltay and Boatwright, this volume). Overall, the GMPEs matched the median level of ground motion and the general distance decay, as well as the scatter in the data (Figure 4). However, for most GMPEs at most periods, the attenuation in the data is stronger than that in the models, most obviously at the shorter periods, i.e. PGA. The DYFI data also indicate higher-than average macroseismic intensities within 20 km of the epicenter and lower than average values at greater distances. This observation likely indicates that the attenuation structure in the Napa and San Joaquin-Sacramento Delta region is stronger than the average attenuation in California, on which the GMPEs were built.

At close distances, within ~20 km, the PGA data compares very well with the GMPEs (Figure 4, left); because stress drop is most closely linked to PGA recordings at nearby

stations, we infer that the South Napa earthquake was of average stress drop, corresponding to ~5MPa (Baltay and Hanks, 2014).

The residual maps show positive residuals (stronger than predicted ground motion) in the north along both the West Napa Fault and in the Sonoma Basin, likely due to the northerly rupture directivity, and along the Rodgers Creek Fault, especially at the longer periods (e.g., Figure 4, right, for PSA of 1.0 s). Additionally, particularly at 1.0 second, there are strong positive residuals at stations to the south of the earthquake, showing a linear feature in the along-strike direction. These may align with a Quaternary-active fault near the Franklin or Southampton Fault, and continuing south to the Calaveras fault If so, they may be indicative of a fault guided wave, indicating that these other structures may be thoroughgoing.

Geodetic Models of Coseismic Slip and Afterslip

Time series from 64 regional continuous GPS (CGPS) sites and 13 campaign or “survey-mode” GPS (SGPS) stations re-occupied within 3 days of the earthquake constrain the coseismic displacement field at earth’s surface. Comparison of the 5-minute kinematic solutions from the CGPS stations, providing the most direct estimates of the coseismic offsets, with 24-hour solutions (Figure 5) indicates that shallow displacements grew an additional 30-50% during the first 24 hours following the earthquake. This afterslip is

best illustrated by horizontal-component time series for P261, the closest CGPS site to the West Napa fault (Figure 6).

Coseismic offsets of a few cm were estimated from the GPS daily position time series for most of the CGPS and SGPS stations (Figure 7). For each station we fit a linear trend (interseismic motion), a coseismic step, and post-earthquake Omori decay (with fixed time constant) using the approach of Langbein (2004) which accounts for temporally correlated noise; for CGPS sites we also included seasonal terms. Using daily positions, combined with the time lag between the earthquake and initial campaign GPS measurements, resulted in the mapping of some postseismic displacement into the coseismic offset estimates. Consistent with its proximity to the fault plane, campaign site DEAL, located 770 m west of the trace of the surface rupture, moved about 23 cm to the NNW. This observation would suggest approximately 46 cm of total slip at the surface in this location.

Synthetic aperture radar (InSAR) data place additional constraint on the coseismic deformation. The earliest repeat pass was obtained on 27 August 2014 by the COSMO SkyMed 2 satellite, which repeated a pass on 26 July 2014. The unwrapped interferogram representing its range change from X band SAR, shown in Figure 8a, reveals a quadrant pattern of deformation consistent with a strike-slip rupture. Since the satellite orbit is descending looking to the west, positive range change is consistent

with either uplift or eastward motion. As for the GPS data, this interferogram contains both coseismic motions and early afterslip.

We inverted the GPS and InSAR data for slip distributions using the Cascading Adaptive Transitional Metropolis in Parallel (CATMIP) algorithm (Minson et al., 2013). The model fault follows the western branch of the mapped surface rupture and is assumed to extend vertically to 12 km depth. We discretized the fault into subfaults that are approximately 1 km in down-dip dimension and 1.5 km in along-strike dimension. Strike slip was given a uniform prior distribution that is truncated at -5 mm to enforce positive (right lateral) motion. The dip slip component was given a Gaussian prior distribution of 0 meters with a standard deviation of 5 mm. We applied spatial averaging to the slip distribution below 1 km depth via a moving arithmetic mean with averaging lengths of three subfaults in the down-dip and along-strike direction.

Figure 9a shows the results of inverting the GPS offsets estimated from the daily position time series, along with coseismic surface rupture measurements (Brooks et al., 2014; Ponti et al., 2014; Trexler et al., 2014), for the surface coseismic slip distribution. The surface slip (Figure 10) and GPS data (Figure 7) are fit reasonably well, and the majority of inferred slip underlies the region experiencing near-fault postseismic displacement. The slip distribution has an Mw 6.1, slightly larger than the Mw 6.0 inferred from seismic data reflecting the inclusion of afterslip into the GPS offsets.

Figure 9b shows the results of jointly inverting the GPS and InSAR data. The fit to the data is shown in Figures 8b and 11. In these inversions we use the approach of Johanson and Burgmann (2010) to determine the relative weighting of GPS and InSAR data. The resulting slip distribution is somewhat complementary to that based solely on the GPS and surface slip data from 24 August, with slip extending deeper as well as in both directions along-strike from the area of inferred peak slip of 24 August. In comparison to the results in Figure 9a, additional moment release with equivalent Mw 5.5 occurred in the three days following the mainshock. The inversion results suggest that some afterslip may have occurred below 1 km depth on the NW half of the fault.

Surface Rupture and Afterslip

The South Napa earthquake was the first earthquake in the San Francisco Bay Area to produce a significant surface rupture since the 1906 San Francisco earthquake. The mapped surface rupture extended along and between mapped Quaternary and Holocene active strands of the West Napa Fault (Figure 1). The earthquake struck in a populated region containing a large number of well-maintained roads and vineyards, which facilitated mapping of the surface rupture. Field reconnaissance began within a few hours of the earthquake and included road surveys as well as helicopter overflights provided by the California Highway Patrol that were coordinated by the CGS-EERI Earthquake Clearinghouse. The mapped surface rupture consisted primarily of a zone of

right-lateral fractures from less to a meter to more than tens of meters wide. Although the rupture varied along the fault, it was usually observed as a zone of echelon left-stepping fractures (Figure 12). Field mapping was assisted by lineaments observed in Synthetic Aperture Radar (SAR) data, initially interferograms of Agencia Spaziale Italiana COSMO-SkyMed data (X-band), NASA/JPL UAVSAR (L-band) data, and the European Space Agency's (C-band) Sentinel-1-A data (GEER, 2014).

The mapped surface rupture extended approximately 12.5 km NNW from the town of Cuttings Wharf in the south to north of Alston Park in the City of Napa (Figure 13). A complex pattern of surface slip was observed along 6 different sub-parallel fault strands. Net surface slip was highest along fault strand A, which was also the longest fault strand that ruptured in the earthquake. A late Quaternary active strand of the West Napa Fault had previously been mapped along the center section of Strand A (Figure 1). The maximum net surface slip along Strand A, about 46 cm, was measured about 10 km NNW of the epicenter and is thought to be entirely co-seismic. Strand C, located east of strand A, was the second longest surface fault rupture and had the second highest amount of surface slip, reaching a maximum of 8 cm in Brown's Valley. Surface slip on the shorter strands B and D to F is also thought to be primarily coseismic and reached a maximum of 6 cm. Surface slip on strand F, on a Holocene active strand of the mapped West Napa Fault at the Napa County Airport (Figure 1), was minor. Surface slip on the other strands of the West Napa Fault east of strand A could have resulted from either triggered slip or surface rupture (Hudnut et al., 2014). The surface slip estimates shown

on Figure 10 represent the earliest measurements made following the earthquake. Nonetheless, some of these measurements may include afterslip.

Within the first 24 hours following the earthquake, afterslip was observed from the ongoing development of surface cracking on roads and other man-made features. To better quantify the afterslip the USGS established four alignment arrays across the fault (Lienkaemper et al., 2014). Afterslip continues to accumulate more rapidly south of the maximum surface coseismic slip locality on strand A, and also to the north of the maximum coseismic slip location, but at a much lower rate than was observed for the first 48 hours following the mainshock (Hudnut et al., 2014; Lienkaemper et al., 2014). Up to 20 cm of right-lateral afterslip was observed within 48 hours of the mainshock, mainly on the southern half of strand A. It is expected that ongoing analysis of imagery, repeat mobile LiDAR, and campaign and continuous GPS data, will provide more information on the amount and location of afterslip along the rupture zone.

Comparison with eleven other moderate California strike-slip earthquakes since 1948 indicates that the South Napa earthquake coseismic surface rupture length and slip were unusually large (Table 1). Eleven other earthquakes, having comparable magnitudes between 5.5 and 6.15 (average M5.9), and comparable focal depths between 5.8 and 14.8 km (average 9.4 km), had an average coseismic surface rupture length of 4.6 km, and an average coseismic surface slip of 4.3 cm. Four of these earthquakes had no coseismic surface rupture and six had coseismic surface slips of 1

cm or less. In contrast, the South Napa earthquake produced a surface rupture length nearly 3 times larger than the average surface rupture length and a coseismic surface slip that is 14 times larger than the average slip. The observed surface afterslip for the South Napa earthquake, up to 35 cm, is also several times higher than the average of 5.1 cm.

Paucity of Ground Failure

Few observations of liquefaction, landslides, or other ground failures were identified in reconnaissance surveys following the earthquake. Sand boils were noted in the Napa River channel in Napa at the Third Street Bridge (GEER, 2014). Some failures of road cuts and dislodged boulders were noted to the northwest of the epicenter (Walter Mooney, written comm., 2014). These findings are in accord with the compilation by Youd and Hoose (1978) that does not report ground failures in Napa Valley produced by historical earthquakes in Northern California, including the 1892 Vacaville, 1898 Mare Island, and 1906 San Francisco earthquakes. Youd and Hoose (1978) noted that the April 1906 San Francisco earthquake was preceded by an above average rainy season and a month of exceptionally heavy rainfall in March, yet those authors found no reports of ground failures in 1906 in the Napa Valley.

The relative scarcity of ground failures during the 2014 South Napa earthquake may partly reflect the low groundwater table resulting from the occurrence of the

earthquake near the end of the dry season and a three-year-long drought. The South Napa earthquake occurred near the end of the summer dry season with no appreciable rain being measured in Napa for nearly 4 months, since April 25 (Napa County University of California Cooperative Extension, 2015). Total rainfalls in Napa during the two rainy seasons prior to the earthquake were 70% and 53% of average, respectively (Napa County University of California Cooperative Extension, 2015). The USGS stream gage record for the Napa River shows that in the month before and on the day of the earthquake the stream levels were lower than since before January 2008 and that stream discharge rates were at low levels (1.6 ft^3/s) (USGS, 2015).

Although we have not systematically reviewed records of groundwater levels in Napa Valley, a preliminary review of data from several selected water wells in the Napa area (CA Department of Water Resources, 2015) indicates that the seasonal variation in the depth to the top of ground water in Napa Valley is in the range of 2 to 12 m (6 to 40 feet), and that depths to the tops of groundwater tables approach their lowest point at the end of August. One water well, located in the center of Napa Valley about 4.3 km north of downtown and 0.6 km west of Napa River, shows that groundwater levels have dropped about 1.4 m since 2006, and at the time of the South Napa earthquake the water level in this well was at depth of 13.4 m. Many practitioners consider triggering of liquefaction at depths more than about 13 to 16 m to be uncommon, and should it occur, it is unlikely to deform the ground surface. We believe that the low groundwater

table in Napa Valley at the time of the earthquake reduced the saturation of the young sands and sandy deposits and inhibited liquefaction.

We also considered the liquefaction susceptibility of deposits in Napa Valley when saturated. Jennifer Thornburg of the California Geological Survey (oral comm., 2015) has reviewed borehole logs from Napa Valley on file at CGS and has identified few liquefiable deposits. She found that the young deposits are typically too fine grained to be liquefiable. We speculate that the low gradients of streams in the center of Napa Valley and the potential absence of suitable coarser grained materials sourced from the surrounding hills (volcanic bedrock in the hills tend to weather to finer grained material) may contribute to the absence of deposits prone to liquefaction.

Finally, as noted by Seed et al. (1983) from a liquefaction viewpoint, “the main difference between different magnitude events is the number of cycles of stress which they induce.” The South Napa earthquake produced only 2 to 4 stress cycles in the strong ground motions in downtown Napa (Station N016), fewer than expected for a M6 earthquake (5-6 cycles).

Site Response

Comparison of the mapped red- and yellow-tagged structures with the mapped surface geology in Figure 1 indicates that the majority of these damaged buildings were built on three main soil types (Witter et al., 2006): Historic alluvial deposits from the Napa River and Napa Creek (Qhc), Holocene alluvial deposits (Qha), and Holocene fan deposits (Qhf2). There is a suggestion in Figure 1 that the boundary between Latest Pleistocene and Holocene fan deposits marks the northern boundary of the red- and yellow-tags in northern Napa, apart from tags in the older fan deposits associated with mobile home parks. Boatwright et al. (this volume) notes a correlation of the locations of these damaged structures with the isocontours of the thickness of the Napa Basin. It seems likely that the deposits in the Napa Basin amplified the ground motions in the city of Napa and contributed to the damage there.

Temporary seismic stations were deployed by the USGS in the Napa region to record aftershocks (Figure 1). A valley-crossing, east-trending deployment of 6 stations was made near the northern limit of the surface rupture. A north-trending deployment of 7 stations was made along the trend of the Napa Valley. Five sites were deployed in downtown Napa to investigate the spatial variability of the strong shaking at a finer scale. The California State University East Bay deployed 3 stations in Napa that complemented these arrays (not shown in Figure 1). Finally, dense arrays of instruments were deployed across three separate fault strands to record fault zone guided waves to investigate the connectivity of the fault strands (Catchings et al., 2014).

A comparison of the aftershock recordings from 5 stations in downtown Napa reveals little variation in site response over a distance of a km (Hudnut et al., 2014).

Discussion

The M6.0 South Napa earthquake, the largest in the San Francisco Bay Area in 25 years, occurred on the West Napa Fault system, a known but relatively minor dextral strike-slip fault lying between the larger Rodgers Creek and Green Valley faults. The earthquake is a reminder not only that magnitude M6.0 earthquakes can occur on relatively minor fault systems throughout the Bay Area, and California, and that often these minor fault systems have not been well characterized. Another lesson is that earthquakes of this magnitude can cause substantial ground motions resulting in significant damage to buildings that were not built to current building code standards. Fortunately, the EERI field team survey reported that buildings that had been retrofit generally fared better than those that had not (EERI, 2014). This point is well-illustrated by the recording made by a USGS NetQuakes seismometer in downtown Napa of PGA of 61% g at the foundation level of an masonry building that had been retrofit and suffered essentially no damage (Erol Kalkan, written comm., 2014).

The earthquake produced an unusual amount of surface rupture, triggered slip, and afterslip for its magnitude. Although using UAVSAR and other SAR imagery to guide the

field mapping of surface rupture and deformation was not novel, the field mapping and imagery were unusually well integrated for this earthquake. The monitoring of afterslip with repeat photography, alignment arrays, mobile LiDAR, repeat SAR imagery, and GPS is ongoing but represents a standard of practice that should be used following future surface rupturing earthquakes.

The focal mechanism and mapping of the surface rupture helped to document the SW dipping fault plane of the mainshock. The aftershocks also appear to define a NE dipping fault plane, of more moderate dip, that intersects the mainshock fault plane at a depth of about 9 to 10 km. The intersection of these faults causes a well-resolved south dipping streak of seismicity and may give clues for the origin of other linear seismicity streaks observed elsewhere.

Finally, we note that the South Napa earthquake was well recorded by seismometers and accelerometers and produced a useful set of strong motion data in the near-field that have engineering implications. These recordings are a testament to the steady investment in upgrading seismic instrumentation and the benefits that are derived from this investment, including Earthquake Early Warning.

Acknowledgements:

We would like to acknowledge financial support from the Earthquake Hazards Program of the USGS and from the CGS. Anne Rosinski, CGS, coordinated the CGS Earthquake Clearinghouse at Napa. Mike Oskin at UC Davis and his students conducted initial mapping used to help define the surface rupture. We acknowledge with gratitude the contributions of the many individuals who assisted following the earthquake. For permanent network operations: Dave Croker, Lynn Dietz, Walt Jungblut, Fred Klein, Will Kohler, John Krueger, John Lee, Jim Luetgert, Harold Macbeth, Jonah Merritt, David H. Oppenheimer, Salvador Robles, Jim Smith, Nick Stein, Chris Stephens, Robert Summers, Roy Tam, and Jack Tomey. For assistance in field mapping: Mike Bennett, Steve B. Delong, Suzanne Hecker, Thomas L. Holzer, Alexandra Pickering, John Tinsley, Nikita Avdievitch, Carol Prentice, Carla Rosa, and Robert Sickler. Geodetic monitoring: Chris Guillemot, John Langbein, Eleyne Phillips, Jim Sutton, Jerry Svarc, and Chuck Wicks. For the aftershock deployment: Rufus Catchings, Coyn Criley, Shane Detweiler, Russell Sell, Jemille Erdem, Lind Gee, John Hamilton, Alena Leeds, Steve Ploetz, Steve Roberts, Joe Svitek, and Dave Wilson. Bill Ellsworth, Robert Graves, Tom Parsons, Ross Stein, and an anonymous journal reviewer reviewed earlier drafts of this paper.

Project in part carried out using CSK® products, © ASI (Italian Space Agency), delivered under the ASI license provided under the Caltech/JPL-ASI/CIDOT CaliMap project. Continuous GPS data used in this study were recorded by instruments of the Plate Boundary Observatory (PBO,http://pbo.unavco.org/) and the Bay Area Regional Deformation (BARD) network (http://seismo.berkeley.edu/bard/). The PBO is operated

by UNAVCO for EarthScope (www.earthscope.org) and supported by the National Science Foundation (No. EAR-0350028 and EAR-0732947). Any use of trade, firm, or product names is for descriptive purposes only and does not imply endorsement by the U.S. Government.

Data availability

Data from ShakeMap, available for download at http://earthquake.usgs.gov/earthquakes/eventpage/nc72282711#shakemap. Vs30 values at each station are taken from the NGA-West2 database (preferred; available at) or the grid.xml file available with the ShakeMap, if the station is not in the NGA-West2 database.

Recorded strong motion data are available at the Center for Engineering Strong Motion Data (http://strongmotioncenter.org/cgi-bin/CESMD/iqr_dist_DM2.pl?iqrID=SouthNapa_24Aug2014_72282711&SFlag=0&Flag=2).

The moment tensor solution is from: (http://www.ncedc.org/mt/nc72282711 MT.html)

GPS data are available from: (http://earthquake.usgs.gov/monitoring/gps/SFBayArea/)

References

Abrahamson, N., W. Silva, and R. Kamai (2014). Summary of the ASK14 ground-motion relation for active crustal regions, Earthquake Spectra **30**, 1025-1055.

Armstrong, C.F. (1979). Coyote Lake earthquake, August 6, 1979, California Geology **32**, 248-251.

Bakun, W. H. (1999). Seismic activity in the San Francisco Bay region, Bull. Seismol. Soc. Am. **89**, 764–784.

Baltay, A. S. and T. C. Hanks (2014). Understanding the magnitude dependence of PGA and PGV in NGA-West2 Data, Bull. Seismol. Soc. Am. 104, 6, doi: 10.1785/0120130283

Baltay, A. S and J. Boatwright (2015). Ground motion observations of the 2014 South Napa earthquake, Seismol. Res. Lett., this volume.

Boatwright, J., J.L. Blair, B. T. Aagaard, and K. Wallis (2015). The distribution of red and yellow tags in the City of Napa, Seismol. Res. Lett., this volume.

Boore, D. M, J. P. Stewart, E. Seyhan, and G. M. Atkinson (2014). NGA-West2 equations for predicting PGA, PGV, and 5%-damped PSA for shallow crustal earthquakes, *Earthquake Spectra* ***30***, 1057-1085, doi: 10.1193/070913EQS184M.

Bonilla, M. G., J. J. Lienkaemper, and J. C. Tinsley (1980). Surface faulting near Livermore, California, associated with the January 1980 earthquakes, U.S. Geol. Surv. Open-File Rept. 80-523, 27 p.

Brooks, B., K. Hudnut, C. Glennie, and T. Ericksen (2014). Near-field deformation associated with the M6.0 South Napa earthquake surface rupture, Abstract S33F-4900 presented at 2014 Fall Meeting, AGU, San Francisco, Calif., 15-19 Dec.

Brossy, C., K. Kelson, and M. Ticci (2010). Digital compilation of data for the Contra Costa Shear Zone for the northern California Quaternary fault map database: Collaborative research with William Lettis & Associates, Inc. and the U.S. Geological Survey, Award No. 07HQGR0063, 13 pp., 4 figures, http://earthquake.usgs.gov/research/external/reports/07HQGR0063.pdf.

CA Department of Water Resources (2015): http://www.water.ca.gov/waterdatalibrary/groundwater/hydrographs/index.cfm

Campbell, K. W., and Y. Bozorgnia (2014). NGA-West2 ground motion model for the average horizontal components of PGA, PGV, and 5%-damped linear acceleration response spectra, *Earthquake Spectra **30***, 1087-1115, doi: 10.1193/070913EQS175M.

Catchings, R., M. Goldman, G. Slad, C. Criley, J. Chan, R. Fay, W. Fay, and J. Svitek (2014). Continuity of the West Napa Fault Zone inferred from aftershock recordings on fault-crossing arrays, *AGU 2014 Fall Meeting abstract #S31G-08,* San Francisco, Calif., 15-19 Dec.

Chiou, B. S. J., and R. R. Youngs (2014). Update of the Chiou and Youngs NGA model for the average horizontal component of peak ground motion and response spectra, *Earthquake Spectra **30**,* 1117-1153, doi: 10.1193/070913EQS219M.

d'Alessio, M. A., I. A. Johanson, R. Bürgmann, D. A. Schmidt, and M. H. Murray (2005). Slicing up the San Francisco Bay Area: Block kinematics and fault slip rates from GPS-derived surface velocities, J. Geophys. Res. **110**, B06403, doi:10.1029/2004JB003496.

EERI (2014). M 6.0 South Napa earthquake of August 24, 2014, EERI Special Earthquake Report, October 2014, 27 pp. http://www.eqclearinghouse.org/2014-08-24-south-napa/preliminary-reports/

Ellsworth, W.L. (1990). Earthquake History, 1769-1989, chap. 6 *of* Wallace, R.E., ed., The San Andreas fault System, California, U.S. Geol. Surv. Prof. Paper 1515, p. 152-187.

Felzer, K.R. (2013). Appendix K-the UCERF3 earthquake catalog, U.S. Geol. Surv. Open-File Rept. 2013–1165, Calif. Geol. Surv. Special Rept. 228, and Southern California Earthquake Center Publication 1792.

Field, E.H., G.P. Biasi, P. Bird, T.E. Dawson, K.R. Felzer, D.D. Jackson, K.M. Johnson, T.H. Jordan, C. Madden, A.J. Michael, K.R. Milner, M.T. Page, T. Parsons, P.M. Powers, B.E. Shaw, W.R. Thatcher, R.J. Weldon, II, and Y. Zeng (2013). Uniform California earthquake rupture forecast, version 3 (UCERF3)—The time-independent model: U.S. Geol. Surv. Open-File Rept. 2013–1165, 97 p., California Geol. Surv. Special Rept. 228, and Southern California Earthquake Center Publication 1792, http://pubs.usgs.gov/of/2013/1165/.

GEER (2014). August 24, 2014 South Napa, California Earthquake, GEER Association Report No. GEER-037, Section G, http://www.geerassociation.org/GEER_Post%20EQ%20Reports/SouthNapa_2014/index.html.

Given, D. D., E.S. Cochran, T. Heaton, E. Hauksson, R. Allen, P. Hellweg, J. Vidale, and P. Bodin (2014). Technical implementation plan for the ShakeAlert production system: an Earthquake Early Warning system for the West Coast of the United States, U.S. Geol.

Surv. Open-File Rept. 2014-1097, 31 pages

Graymer, R.W., D.L. Jones, and E.E. Brabb (2002). Geologic map and map database of northeastern San Francisco Bay Region, California: U.S. Geol. Surv. Misc. Field Studies Map MF-2403, version 1.0, scale 1:100,000.

Graizer, V. and E. Kalkan (2015). Update of the Graizer-Kalkan ground-motion prediction equations for shallow crustal continental earthquakes: U.S. Geol. Surv. Open-File Rept. 2015-1009, p. 98.

Hardebeck, J. L., A. J. Michael, and T. M. Brocher (2007). Seismic velocity structure and seismotectonics of the Eastern San Francisco Bay Region, California, Bull. Seismol. Soc. Am. **97**, 826–84.

Hardebeck, J.L., and D.R. Shelly (2014). Aftershocks of the 2014 M6 South Napa Earthquake: Detection, Location, and Focal Mechanisms, Abstract S33F-4927, presented at 2014 Fall Meeting, AGU, San Francisco, Calif., 15-19 Dec.

Hill, R. L., J. A. Treiman, J. W. Given, J. C. Pechman, J. R. McMillan, and J. E. Ebel (1980). Geologic study of the Homestead Valley earthquake swarm of March 15, 1979, California Geology **33**, 60-67.

Hough, S.E. (2014). Where was the 1898 Mare Island earthquake? Insights from the 2014 South Napa earthquake, *AGU 2014 Fall Meeting abstract #S44D-03,* San Francisco, Calif., 15-19 Dec.

Hudnut, K.W., L. Seeber, and T. Rockwell (1989). Slip on the Elmore Ranch fault during the past 330 years and it's relation to slip on the Superstition Hills fault, Bull. Seismol. Soc. Am. **79**, 330-341.

Hudnut, K.W., T.M. Brocher, C.S. Prentice, J. Boatwright, B.A. Brooks, B.T. Aagaard, J.L. Blair, J. Fletcher, J.E. Erdem, C.W. Wicks, J.R. Murray, F.F. Pollitz, J. Langbein, J. Svarc, D.P. Schwartz, D.J. Ponti, S. Hecker, S. DeLong, C. Rosa, B. Jones, R. Lamb, A. Rosinski, T.P. McCrink, T.E. Dawson, G. Seitz, R.S. Rubin, C. Glennie, D. Hauser, T. Ericksen, D. Mardock, D.F. Hoirup, and J.D. Bray (2014). Key recovery factors for the August 24, 2014, South Napa earthquake, U.S. Geol. Surv. Open-File Rept. 2014–1249, 51 p., *http://dx.doi.org/10.3133/ofr20141249*.

Jennings, C.W. (1994). Fault activity map of California and adjacent areas with locations and ages of recent volcanic eruptions, Department of Conservation, California Geol. Surv., Geologic Data Map No. 6, scale 1:750,000.

Johanson, I. A., and R. Bürgmann (2010). Coseismic and postseismic slip from the 2003 San Simeon earthquake and their effects on backthrust slip and the 2004 Parkfield earthquake, J. Geophys. Res. **115**, B07411, doi:10.1029/2009JB006599.

Kelson, K.I., J.N. Baldwin, J.R. Unruh, and W.R. Lettis (2004). Coastal marine terraces define Late Quaternary fault activity and deformation within northern East Bay hills, San Francisco Bay region, Eos Trans. AGU, 85(47), Fall Meeting Supplement, Abstract T13C-1396.

Kelson, K.I., J.R. Unruh, and J.N. Baldwin (2005). Late Quaternary deformation in the northeastern East Bay hills, San Francisco Bay region [abs.], Geological Society of America Abstracts with Programs, v. 37, no. 4, p. 106 http://gsa.confex.com/gsa/2005CD/finalprogram/abstract_85559.htm

Langbein, J. (2004). Noise in two-color electronic distance meter measurements revisited, J. Geophys. Res. **109**, B04406, doi:10.1029/2003JB002819.

Langbein, J., J. R. Murray, and H. A. Snyder (2006). Coseismic and initial postseismic deformation from the 2004 Parkfield, California, earthquake observed by Global Positioning System, creepmeters, and borehole strainmeters, Bull. Seismol. Soc. Am. **96**, S304–S320.

Langenheim, V. E., R.W. Graymer, and R.C. Jachens (2006). Geophysical setting of the 2000 ML 5.2 Yountville, California, earthquake, Implications for Seismic Hazard in Napa Valley, California, Bull. Seismol. Soc. Am. **96**, p. 1192-1198.

Lienkaemper, J.J., and W.H. Prescott (1986). Historic surface slip along the San Andreas Fault near Parkfield, California, J. Geophys. Res. **94**, 17647-17670.

Lienkaemper, J.J., B. Baker, and F.S. McFarland (2006). Surface slip associated with the 2004 Parkfield, California, earthquake measured on alinement arrays, Bull. Seismol. Soc. Am. **96**, S239-S249, doi: 10.1785/0120050806

Lienkaemper, J. J., B. A. Brooks, S. B. DeLong, C. J. Domrose, and C. M. Rosa (2014). Surface slip associated with the 2014 South Napa, California earthquake measured on alinement arrays, *AGU 2014 Fall Meeting abstract #S33F-4898*.

Minson, S. E., M. Simons, and J. L. Beck (2013). A Bayesian approach to finite fault earthquake modeling I: Theory and synthetics, Geophys. J. Int. **194**, 1701-1726.

Napa County University of California Cooperative Extension (2015). http://cenapa.ucanr.edu/about/weather/?weather=station&station=109

Ogata, Y. (1988). Statistical models for earthquake occurrences and residual analysis for point processes, J. Am. Stat. Assoc. **83**, 9-27.

Oppenheimer, D. H., W. H. Bakun, and A. G. Lindh (1990). Slip partitioning of the Calaveras fault, California, and prospects for future earthquakes, J. Geophys. Res. **95**, 8483-8498.

Ouillon, G., C. Ducorbier, and D. Sornette (2008). Automatic reconstruction of fault networks from seismicity catalogs, three-dimensional optimal anisotropic dynamic clustering, J. Geophys. Res. **113**, 15 pp., B01306, doi: 10.1029/2007JB005032.

Parsons, T., M. Segou, V. Sevilgen, K. Milner, E. Field, S. Toda, and R.S. Stein (2014). Stress-based aftershock forecasts made within 24 hours post-mainshock: Expected north San Francisco Bay area seismicity changes after the 2014 M=6.0 West Napa earthquake, *Geophys. Res. Letts*. 41, doi:10.1002/2014GL062379.

Ponti, D., T. Dawson, T., D. Schwartz, B. Brooks, S. DeLong, S. Hecker, K. Hudnut, K. Kelson, J. Lienkaemper, C. Prentice, C. Rosa, R. Rubin, G. Seitz, R. Sicker, and J. Wesling (2014). Surface fault rupture from the M6.0 South Napa earthquake of Aug. 24, 2014, Abstract S33F-4901 presented at 2014 Fall Meeting, AGU, San Francisco, Calif., 15-19 Dec.

Richter, C.F., C.R. Allen, and J.M. Nordquist (1958). The Desert Hot Springs earthquakes and their tectonic environment, Bull. Seismol. Soc. Am. **48**, 315-337.

Rymer, M.J. (2000). Triggered surface slips in the Coachella valley area associated with the 1992 Joshua Tree and Landers, California, earthquakes, Bull. Seismol. Soc. Am. **48**, 832-848.

Seed, H. B., I. M. Idriss, and I. Arrango (1983). Evaluation of liquefaction potential using field performance data, Journal of Geotechnical Engineering, 109, 458-482.

Seyhan, E., and J. P. Stewart (2014). Semi-empirical nonlinear site amplification from NGA-West 2 data and simulations, Earthquake Spectra **30**, no. 3, 1241–1256, doi: 10.1193/063013EQS181M.

Sharp, R.V., M.J. Rymer, and D.M. Morton (1986). Trace fractures on the Banning fault created in association with the 1986 North Palm Springs earthquake, Bull. Seismol. Soc. Am. **76**, no. 6, pp. 1838-1843.

Thurber C., H. Zhang, F. Waldhauser, J. Hardebeck, A. Michael, and D. Eberhart-Phillips (2006). Three-dimensional compressional wavespeed model, earthquake relocations, and focal mechanisms for the Parkfield, California, region, Bull. Seismol. Soc. Am. **96**, S38–S49.

Toppozada, T. R., C. R. Real, and D. L. Parke (1981). Preparation of isoseismal maps and summaries of reported effects for pre-1900 California earthquakes, Calif. Div. Mines Geol. Open-File Rept. 81-11 SAC, 182 pp.

Trexler, C., A. Morelan, and M. Oskin (2014). Rapid Mapping of Surface Rupture from the South Napa Earthquake, Abstract S31G-01 presented at 2014 Fall Meeting, AGU, San Francisco, Calif., 15-19 Dec.

Unruh, J.R., and K.I. Kelson (2002a). Critical evaluation of the northern termination of the Calaveras fault, eastern San Francisco Bay area, California, unpublished Final Technical Report submitted to the U.S. Geological Survey National Earthquake Hazard Reduction Program, Award Number 00-HQ-GR-0082; dated July, 2002; 28 p.

Unruh, J.R., and K.I. Kelson (2002b). Critical evaluation of the northern termination of the Calaveras fault, eastern San Francisco Bay area, California [abs.], Eos Trans. Fall Meeting Supplement, Abstract T62F-04, p. 1300.

USGS (2015). http://waterdata.usgs.gov/ca/nwis/uv?site_no=11458000

Wald, L. (2012). Earthquake information products and tools from the Advanced National Seismic System (ANSS): U.S. Geol. Surv. Fact Sheet 2006–3050 (revised September 2012), 2 p.

Wesling, J. R., and K. L. Hanson (2008). Mapping of the West Napa Fault zone for input into the Northern California Quaternary Fault Database, Final Technical Report, U.S. Geol. Surv. External Award Number 05HQAG0002, 34 pp., 4 tables, 12 figures, 1 plate, 1 appendix. http://earthquake.usgs.gov/research/external/reports/05HQAG0002.pdf

Witter, R.C, K.L. Knudsen, J.M. Sowers, C.M. Wentworth, R.D. Koehler, and C.E. Randolph (2006). Maps of Quaternary deposits and liquefaction susceptibility in the central San Francisco Bay region, California, U.S. Geol. Surv. Open-File Rept. 2006-1037, digital database by Wentworth, C.M., Brooks, S.K., and Gans, K.D., scale 1:24,000, http://pubs.usgs.gov/of/2006/1037/

Youd, T. L., and S. N. Hoose (1978). Historic ground failures in northern California triggered by earthquakes, U.S. Geol. Surv. Prof. Paper 993, U.S. Govt. Print. Off., Washington, iv, 177 p.

Zhang, H., and C. H. Thurber (2003). Double-difference tomography: the method and its application to the Hayward fault, California, Bull. Seismol. Soc. Am. **93**, 1,875–1,889.

Figure Captions:

Figure 1. Map showing mainshock (red dot), aftershocks, surface rupture (red lines), and locations of permanent (unfilled triangles) and temporary (filled triangles) seismic stations. Aftershocks are taken from Hardebeck and Shelly (2014). Locations of red- and yellow-tagged structures are from Boatwright et al. (this volume). Surficial geology is from Witter et al. (2006). Inset map shows location of the major strike-slip faults in the San Francisco Bay Area.

Figure 2. Slip model resulting from the inversion of seismic broadband data recorded at 6 University of California Berkeley seismic network stations. White circle provides location of the hypocenter.

Figure 3. Relocated hypocenters of the first week of the South Napa earthquake sequence, and fault planes fit to the relocations. (Left) Map view with shaded topography. Symbol size represents earthquake magnitude, and fill color represents depth. Crosses and letters indicate cross-section end points. Red lines show the approximate location of the mapped surface rupture. (Upper right) Along-strike section. Black line indicates the intersection of the two Optimal Anisotropic Dynamic Clustering (OADC) planes. (Lower right) Cross-section views, earthquakes within 1 km of the

sections are shown. Black lines indicate the position of the two OADC planes at the location of the cross-section.

Figure 4. (left) Observed ground motion from the ShakeMap compared to five GMPEs: *Abrahamson et al.* (2014), *Boore et al*. (2014), *Campbell and Bozorgnia* (2014), *Chiou and Youngs* (2014) and *Graizer and Kalkan* (2015). Data are adjusted with the Seyhan and Stewart (2014) site correction to a Vs30=760 m/s; the east and north components are shown separately as well as their geometric mean. Median GMPEs and +/- 1 sigma are shown, calculated for M6.05 and for Vs30=760 m/s, and a strike slip focal mechanism with surface rupture. (right) Spatial residuals from the *Abrahamson et al.* (2014) GMPE for PSA of 1.0 second.

Figure 5. Displacements differenced from pre-earthquake measurements at six CGPS sites using 5-minute kinematic solutions (white vectors) and 24 hour solutions (black vectors). Error ellipses are 95% confidence. The mapped surface rupture is shown by the heavy gray curve, and the earthquake epicenter is indicated by the black star.

Figure 6. East and North component kinematic time series at Plate Boundary Observatory site P261 (see Fig. 7 for location). A slope proportional to the pre-earthquake velocity has been subtracted. The vertical dashed line segments indicate the coseismic offset, and the solid curves are flat pre-earthquake and follow an Omori decay post-earthquake.

Figure 7. GPS offsets for 24 August 2014. Black arrows: estimated from position time series, gray arrows: predicted from slip model shown in Figure 9a. Dark gray curve shows surface trace of model fault. Light gray curve shows location of mapped eastern strand of surface rupture (not included in model). Gray dots show locations of surface offset measurements from 24 August 2014.

Figure 8. COSMO SkyMed interferograms spanning 26 July 2014 – 27 August 2014. Positive line of sight (LOS) displacement corresponds to uplift and eastward movement. Heavy green curve shows surface trace of model fault. Heavy purple curve shows location of mapped eastern strand of surface rupture.

Figure 9. Inferred slip distributions. a) Slip on 24 August 2014 inferred from GPS and surface offset data. Star marks hypocenter. Red dots mark subfaults for which there are one or more surface rupture observations. Purple curve at top of fault marks surface rupture from field mapping. B) Slip from 24 – 27 August 2014 (inclusive of coseismic) inferred from GPS and InSAR data.

Figure 10. Offsets from field measurements of the rupture trace (24 August 2014). Circles: observations; Diamonds: inferred slip from inversion for corresponding locations along model fault surface trace.

Figure 11. GPS offsets for 24 – 27 August 2014 (inclusive of coseismic). Black arrows: estimated from position time series, gray arrows: predicted from slip model shown in Figure 9b. Dark gray curve shows surface trace of model fault. Light gray curve shows location of mapped eastern strand of surface rupture (not included in model).

Figure 12. Left-stepping en echelon fractures characteristic of right-lateral fault displacement at the ground surface. Total fault slip measured near this location was 40-46 cm. Photo taken by Dan Ponti on main rupture strand near Buhman Road on the day following the earthquake.

Figure 13. Map showing traces of tectonic surface faulting (yellow lines) produced by the 24 August 2014 South Napa earthquake from Hudnut et al. (2014). Right-lateral surface displacements, measureable in the field, were observed along traces labeled A-F. Solid lines indicate regions where surface faulting was relatively continuous. Dotted lines indicate regions where surface faulting was discontinuous, diffuse, or had negligible offset. Numbers show the earliest measurements of the maximum measured right-lateral offset at selected sites, rounded to the nearest cm; the measurements, made within two days of the earthquake, but probably includes both coseismic slip and afterslip south of Henry Road. Red star is location of earthquake epicenter.

Table 1. Comparison of Seismological and Surface Faulting Parameters for ~M6 Strike-Slip Earthquakes in California since 1948

Event (year)	Magnitude (M)	Focal Depth D (km)	Coseismic Surface Rupture Length (km)	Coseismic Dmax at Surface (cm)	Creep prior to event	Surface afterslip (cm)	Notes
Desert Hot Springs (1948)	6.0	6.0	0	0	no	nr	M and D (Felzer, 2013). Richter et al (1958) report no surface rupture ; 18 km aftershock zone
Galway Lake (1975)	5.0 M_L	5.8	6.8	1.5	no	nr	M and D (Felzer, 2013). Surface offset data from Hill and Beeby (1977)
Parkfield (1966)	6.0	8.6	0 (SA) 10(SWFZ)	0(SA) 6.6(SWFZ)	yes	31 (SA)	M and D (Ellsworth, 1990). San Andreas creeping at 28 mm/yr. Afterslip along 44 km of main San Andreas (SA) Coseismic slip on Southwest Fracture Zone (SWFZ). Surface offset data from Lienkaemper and Prescott (1989)
Homestead Valley (1979)	4.8 M_L 5.5 4.5 M_L 4.8 M_L	8.3 9.3 8.9 2.0	3.25(HV) 1.5 (JV)	11 1	no	nr	M and D (Felzer (2013). Earthquake swarm with rupture along Homestead Valley (HV) and Johnson Valley (JV) faults; both re-ruptured during 1992 M7.2 Landers event. Surface offset data from Hill et al. (1980)
Coyote Lake (1979)	5.9	8.95	0	0	yes	0.5	M and D (Oppenheimer et al., 1990); 14 km rupture length at depth. Discontinuous surface cracking for 14.4 km is likely afterslip. Surface observations from Armstrong (1979)
Greenville (1980)	5.8	14.8	4-6	≥1	yes	≥1	M and D (Ellsworth, 1990). Pre-event creep at 1-2 mm/yr (Lienkaemper et al.,2013). Total surface slip (coseismic + afterslip) was 2.5 cm (Bonilla et al., 1980). Concurrent rupture of conjugate Las Positias fault.
Morgan Hill (1984)	6.2	8.4	0	0	yes	nr	M and D (Oppenheimer et al., 1990). 25km rupture length at depth (between 4-10km). No unequivocal coseismic surface rupture (Harms et al.,1987)
North Palm Springs (1986)	6.02	10.4	9	<0.1	no	nr	M and D (Felzer, 2013). Discontinuous, en-echelon, left-stepping fractures for 9 km along surface trace Banning strand of SA. Offset data from Sharp et al. (1986) who refer to these as “trace fractures” and interpret them as incipient faulting
Elmore Ranch (1987)	6.04	10.8	10	20	no	nr	M and D (Felzer, 2013). Slip distributed on 6 traces across across 8.5 km-wide zone. Longest is 10 km (Elmore Ranch fault). Cumulative surface Dmax for all traces is 20 cm., average~ 10 cm Surface offset data from Hudnut et al. (1989).
Joshua Tree (1992)	6.15	12.3	0	0	no	nr	M and D (Felzer, 2013). 1.5 km discontinuous, triggered slip on East Wide Canyon fault (Rymer, 2000)
Parkfield (2004)	6.0	7.9	0 (SA) 8 (SWFZ)	<0.2(SA) 6.6(SWFZ)	yes	13-36 SA	M and D (USGS).No measurable coseismic rupture on main San Andreas (SA) but followed by 32 km of discontinuous afterslip varying from 13-36 cm. Coseismic rupture on Southwest Fracture Zone (SWFZ). Offset data from Langbein et al. (2006), Lienkaemper et al. (2006)
South Napa (2014)	6.0	10.7	≥12.5	≥60	no	≥35	M and D (USGS). Rupture involved 5 fault traces; some may be triggered. Longest (western) is a minimum of 12.5km. Afterslip on west trace, primarily along southern 8.5 km; value listed is after 60 days with afterslip ongoing. Coseismic Dmax combines strands A (46 cm), C (8cm) and E (6 cm) traces.

Magnitude (M). Magnitudes are Mw unless noted as M_L. Source is UCERF 3 seismicity catalog (Felzer, 2013) unless otherwise noted.
Focal Depth D (km). Source is UCERF 3 seismicity catalog (Felzer, 2013) unless otherwise noted.
Coseismic surface rupture length (km). Reported length of rupture at the surface at time of event; distinct from afterslip. Where multiple fault traces occurred length listed is for the longest trace.

Coseismic Dmax. Reported maximum coseismic surface displacement. Does not include afterslip.
nr. Not reported.

Figure 1

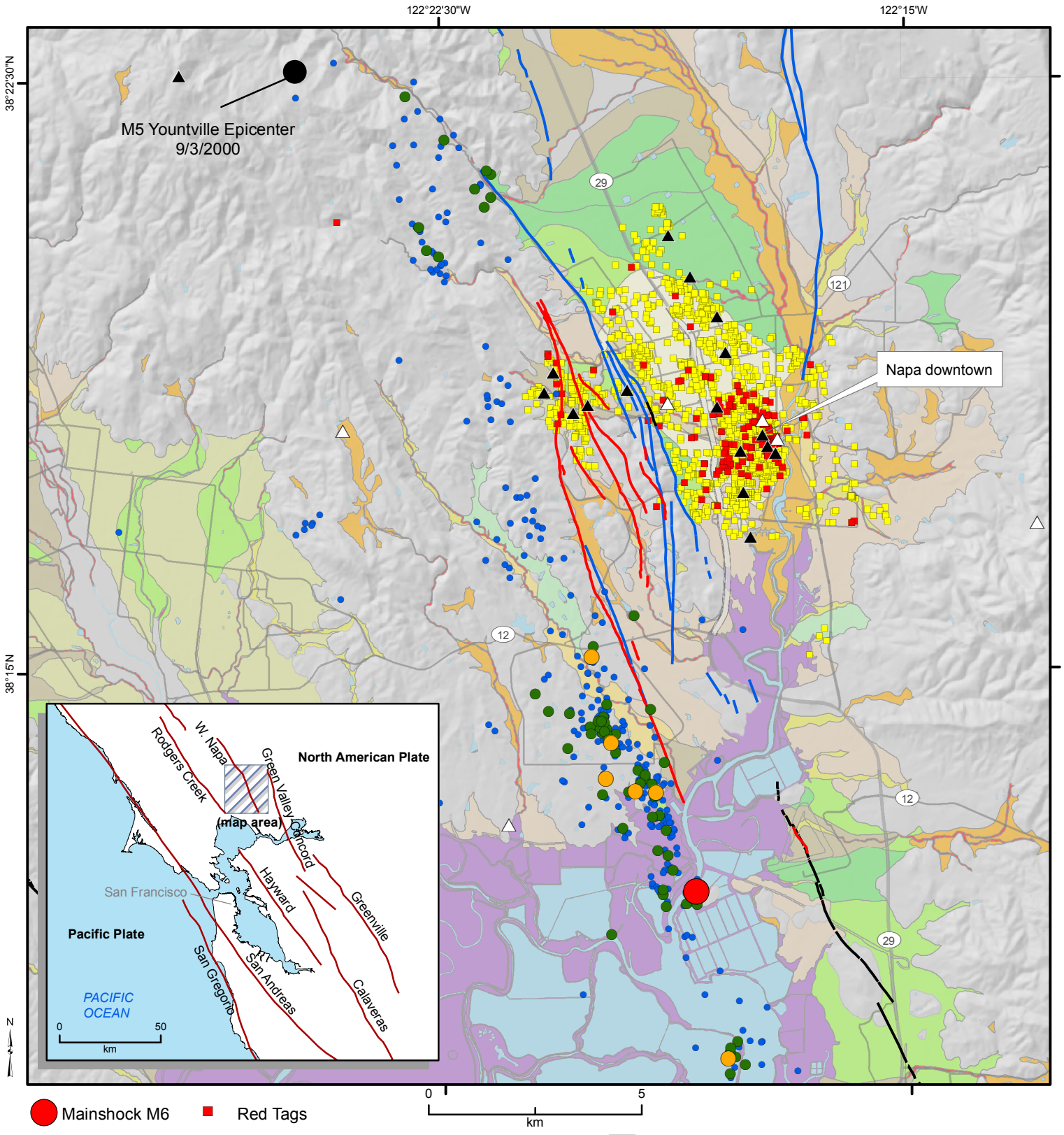
122°22'30"W
122°15'W
38°22'30"N
38°15'N
M5 Yountville Epicenter
9/3/2000
Napa downtown
29
121
12
12
29
North American Plate
Pacific Plate
(map area)
W. Napa
Rodgers Creek
Green Valley
Concord
Hayward
Greenville
San Francisco
San Gregorio
San Andreas
Calaveras
PACIFIC
OCEAN
0
50
km
N
0
5
km
Mainshock M6
M3
M2
M < 2
Red Tags
Yellow tags
Seismic Stations
Temporary
Permanent
New fault rupture
Faults <15,000
Faults <130,000
Historical
Water
adf - Artificial dam fill
Qhc - Historical stream channel deposits
Latest Holocene
Qhty - Stream terrace deposits
Holocene
Qhbm-Qhty - Bay mud and stream terrace deposits
Qhbm - San Francisco Bay mud
Qhf - Alluvial fan deposits
Qhf1 - Younger alluvial fan deposits
Qhf2 - Intermediate alluvial fan deposits
Qhf2-Qpf2 - Intermediate and older alluvial fan
Qht - Stream terrace deposits
Qha - Alluvial deposits, undifferentiated
Holocene to Latest Pleistocene
Qf - Alluvial fan deposits
Qa - Alluvial deposits, undifferentiated
Latest Pleistocene
Qpf - Alluvial fan deposits
Qpf1 - Younger alluvial fan deposits
Qpf2 - Older alluvial fan deposits
Qpa - Alluvial deposits, undifferentiated
Early to Late Pleistocene
Qof - Alluvial fan deposits
Qoa - Alluvial fan deposits, undifferentiated
br - Older deposits and bedrock

Figure 2
Click here to download high resolution image

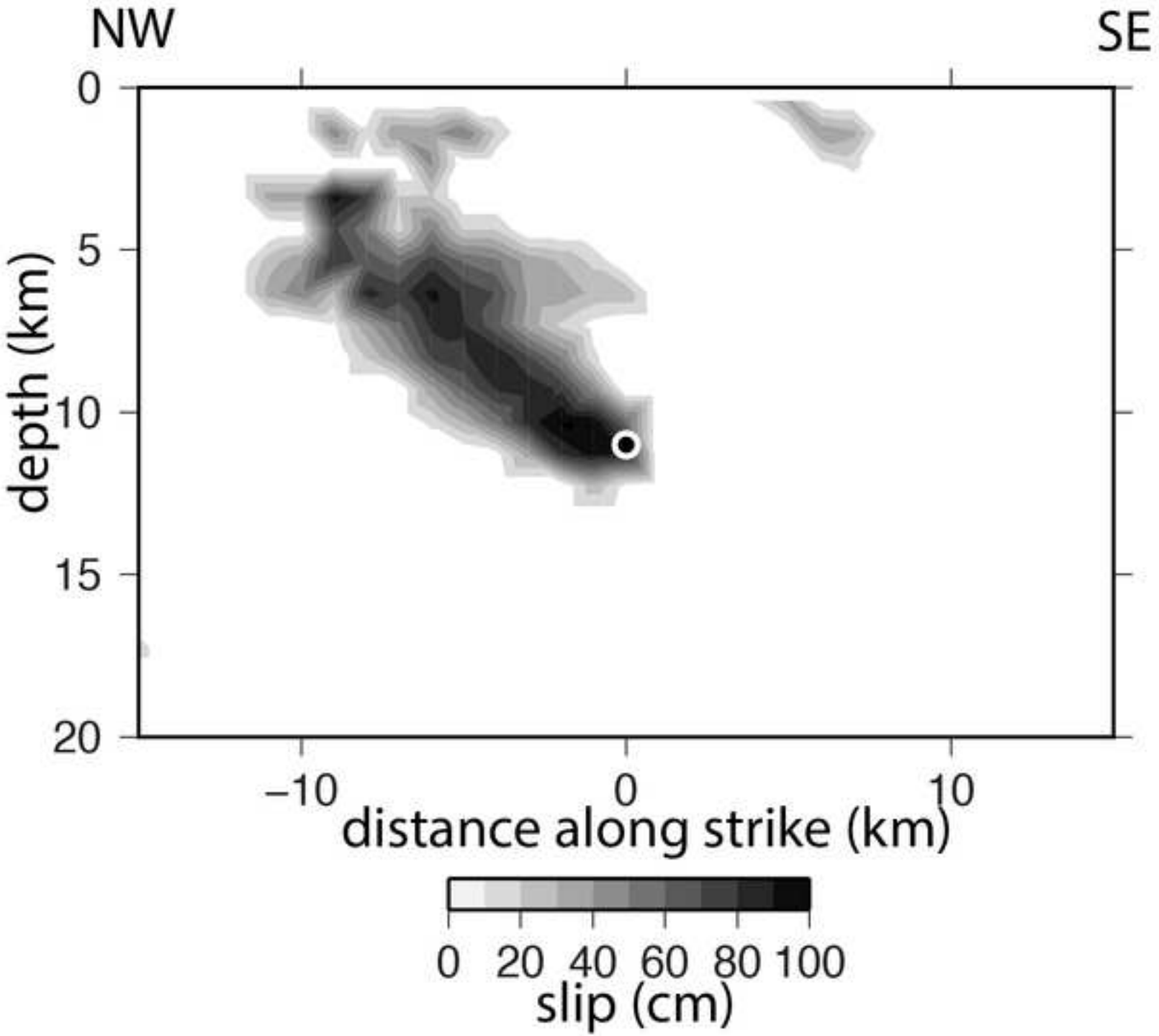

Figure 3

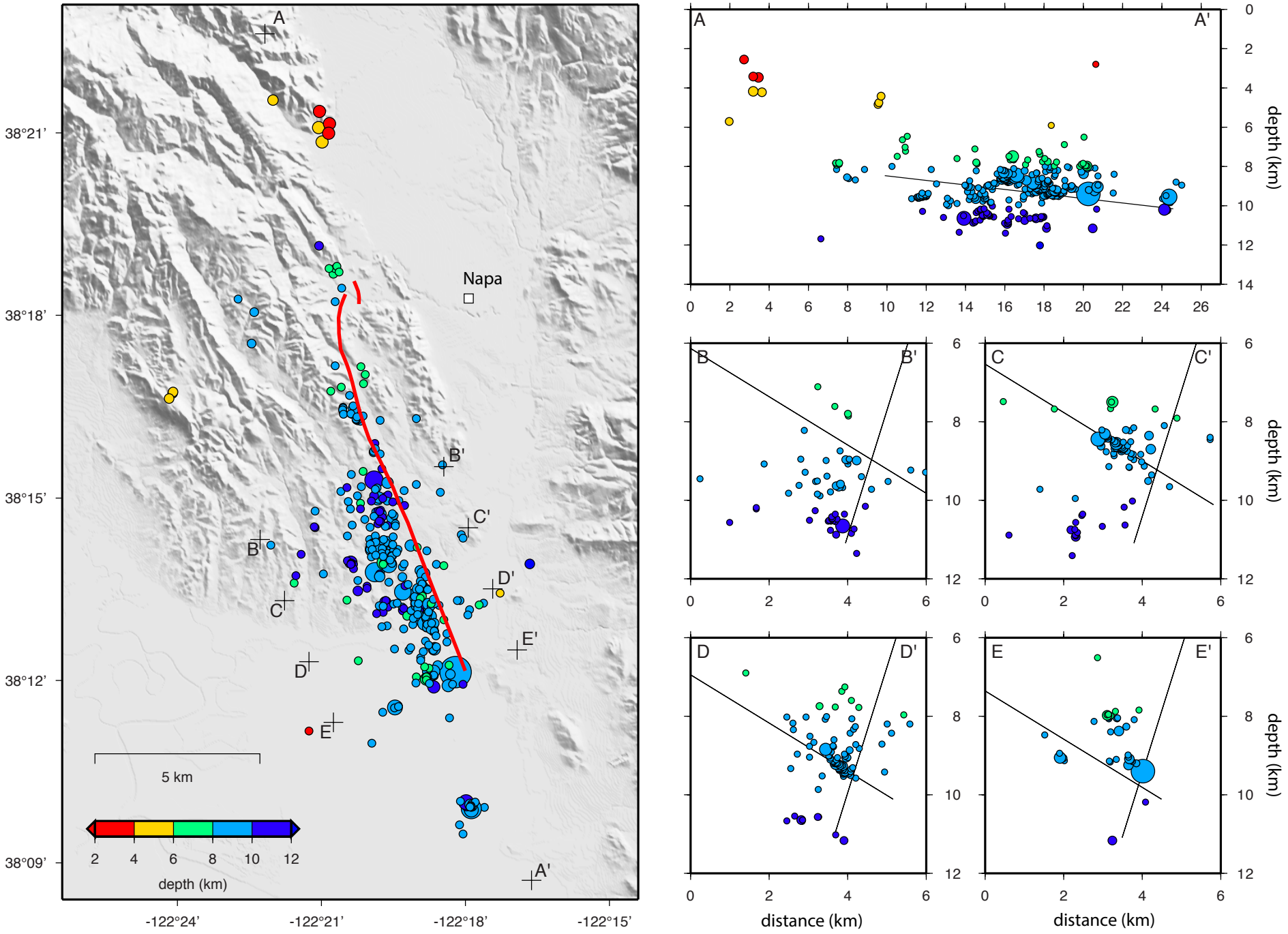
A
A'
B
B'
C
C'
D
D'
E
E'
Napa
38°21'
38°18'
38°15'
38°12'
38°09'
-122°24'
-122°21'
-122°18'
-122°15'
5 km
2 4 6 8 10 12
depth (km)
depth (km)
distance (km)
distance (km)

Figure 4

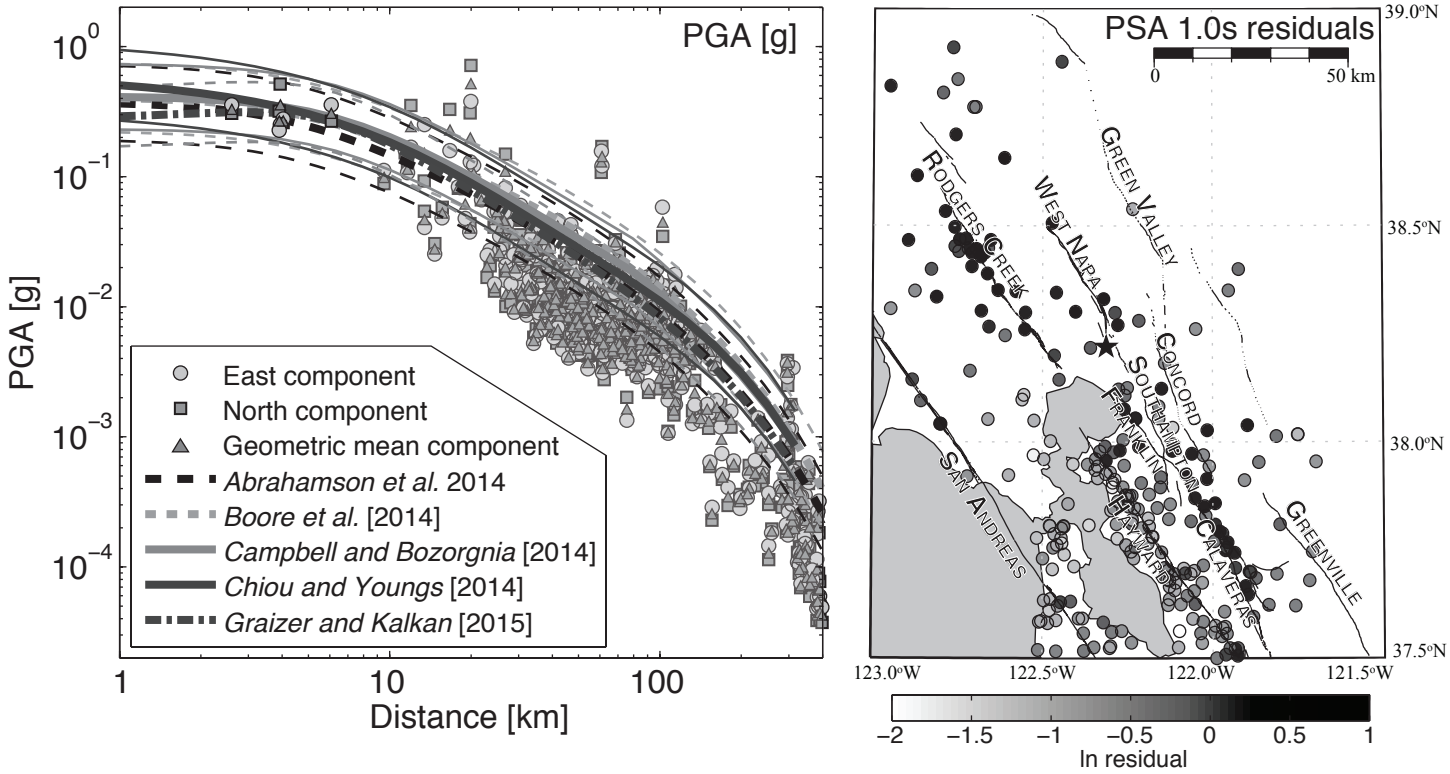
PGA [g]
East component
North component
Geometric mean component
Abrahamson et al. 2014
Boore et al. [2014]
Campbell and Bozorgnia [2014]
Chiou and Youngs [2014]
Graizer and Kalkan [2015]
PGA [g]
Distance [km]
PSA 1.0s residuals
0
50 km
Rodgers Creek
West Napa
Green Valley
Concord
Southampton
Franklin
Calaveras
Greenville
San Andreas
39.0°N
38.5°N
38.0°N
37.5°N
123.0°W
122.5°W
122.0°W
121.5°W
ln residual

Figure 5

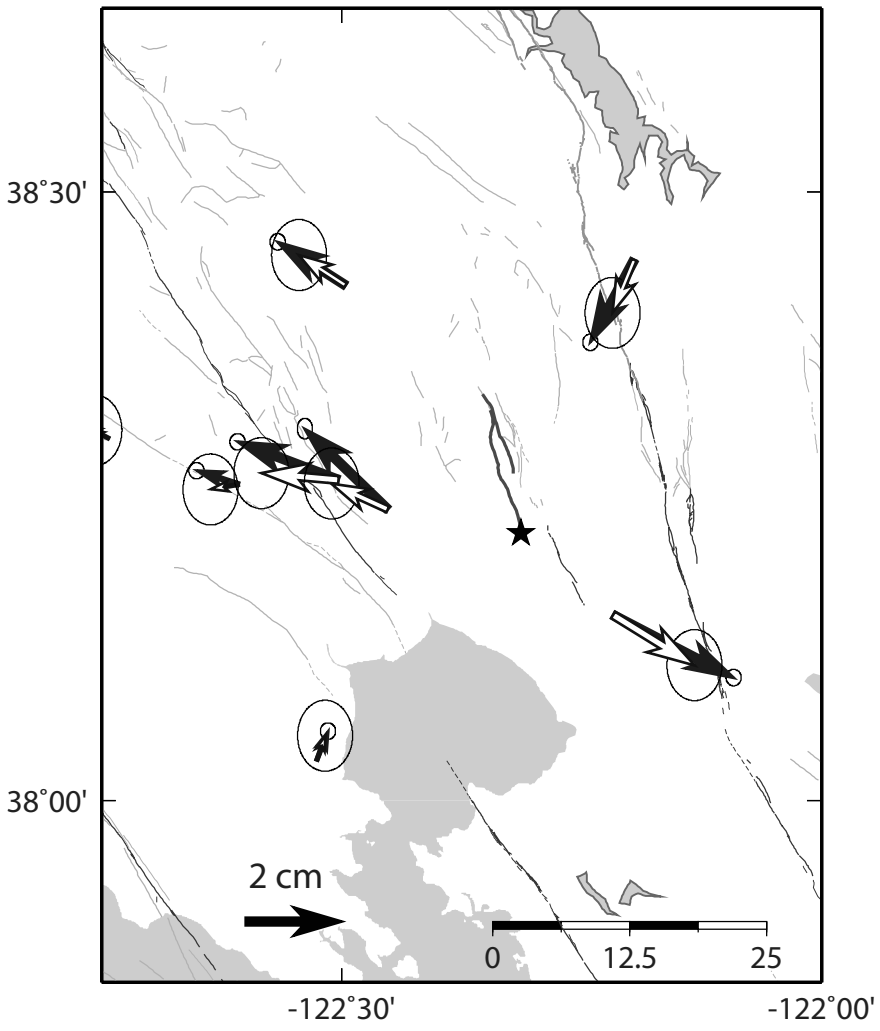

Figure 6

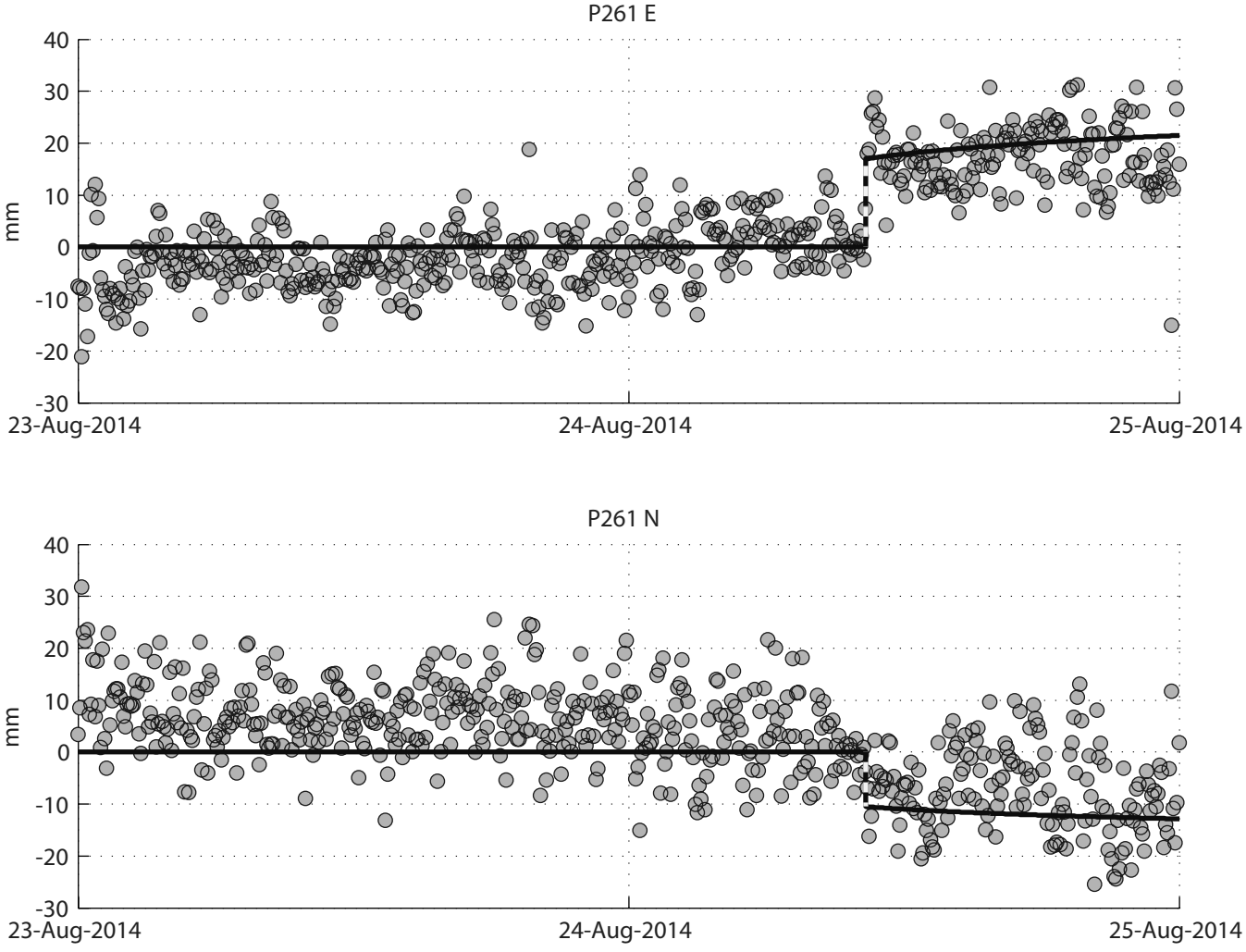
P261 E
40
30
20
10
0
-10
-20
-30
mm
23-Aug-2014
24-Aug-2014
25-Aug-2014
P261 N
40
30
20
10
0
-10
-20
-30
mm
23-Aug-2014
24-Aug-2014
25-Aug-2014

Figure 7

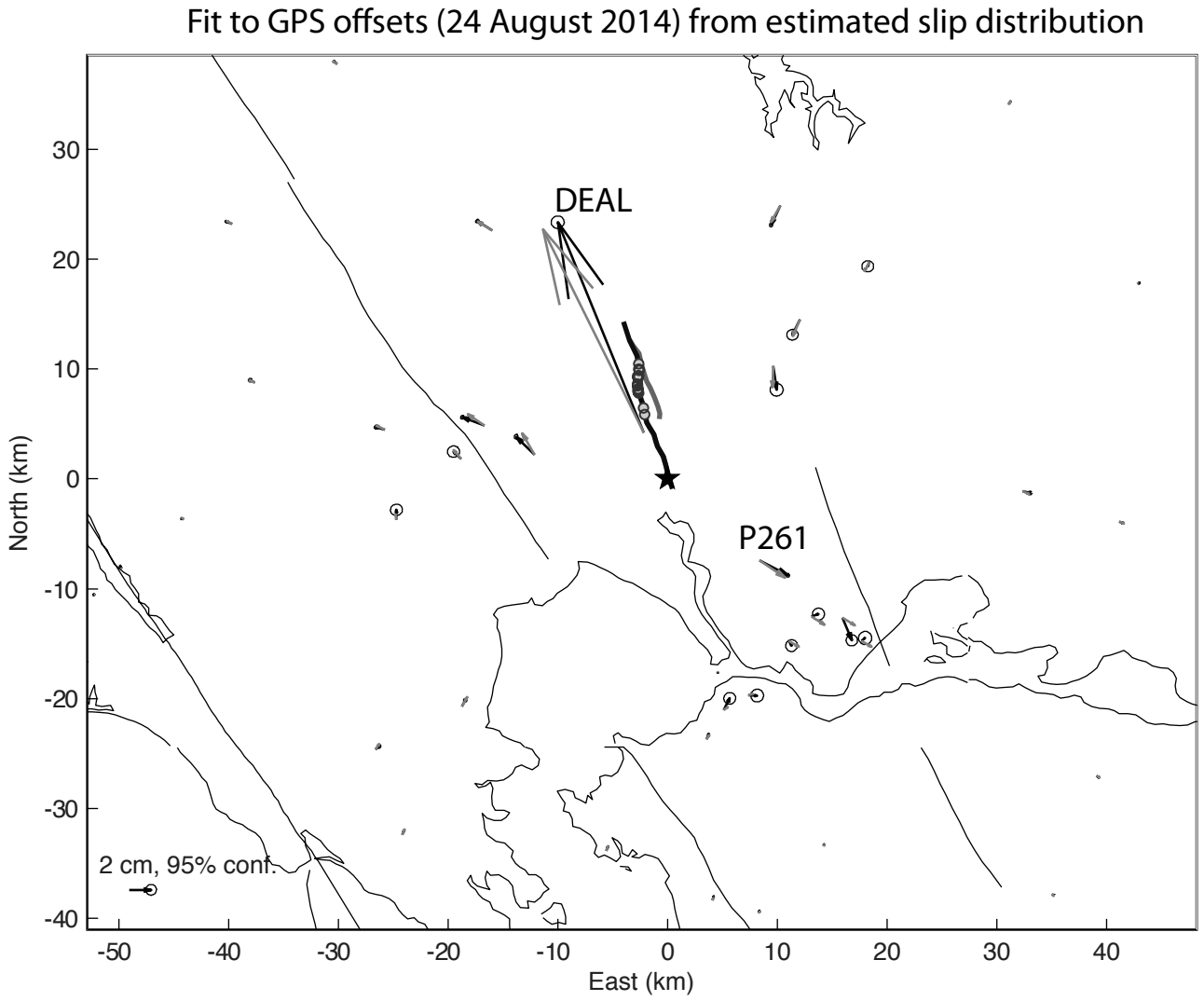
Fit to GPS offsets (24 August 2014) from estimated slip distribution
DEAL
P261
2 cm, 95% conf.
North (km)
East (km)
30
20
10
0
-10
-20
-30
-40
-50
-40
-30
-20
-10
0
10
20
30
40

Figure 8

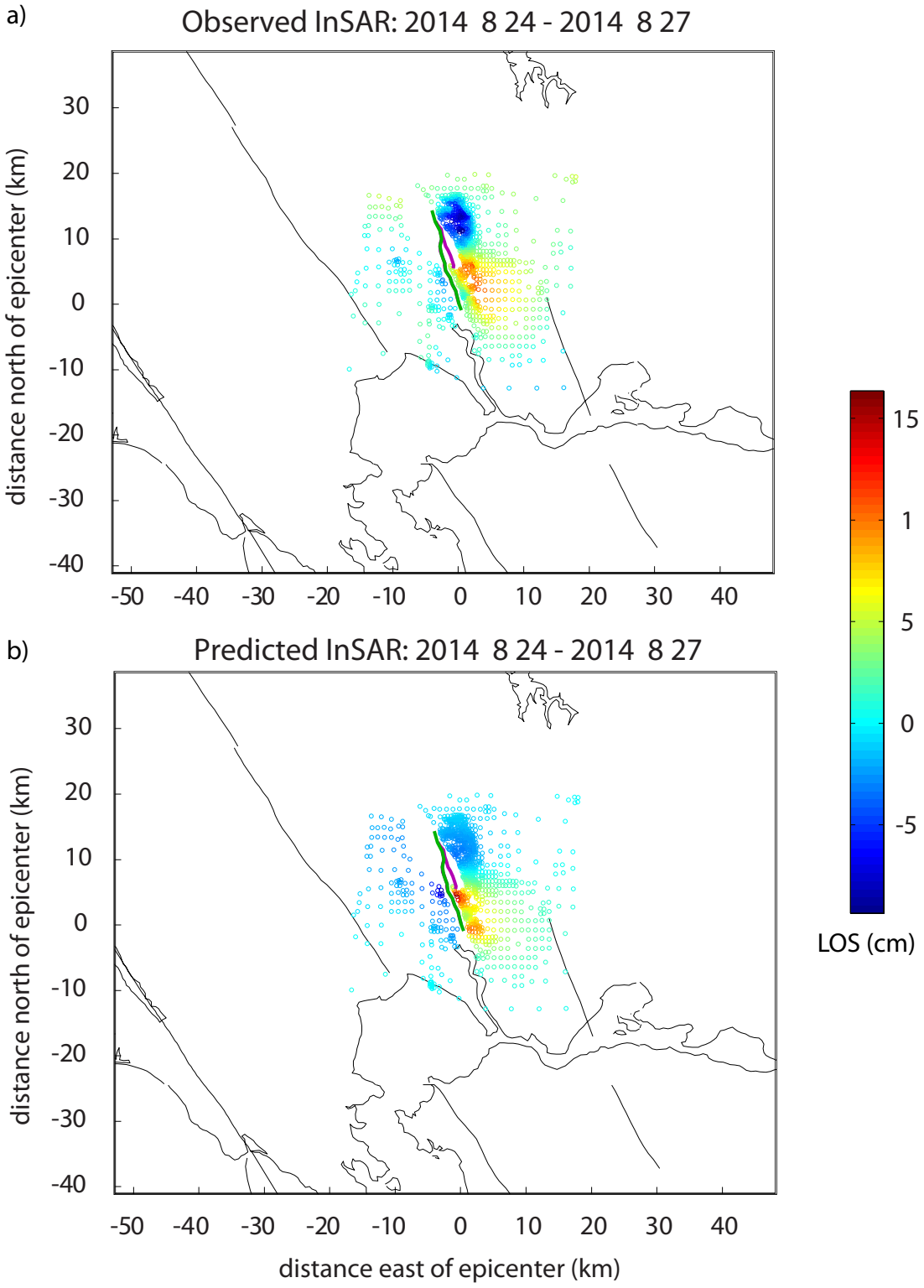
a)
Observed InSAR: 2014 8 24 - 2014 8 27
b)
Predicted InSAR: 2014 8 24 - 2014 8 27
distance north of epicenter (km)
distance east of epicenter (km)
30
20
10
0
-10
-20
-30
-40
-50
40
15
1
5
0
-5
LOS (cm)

Figure 9

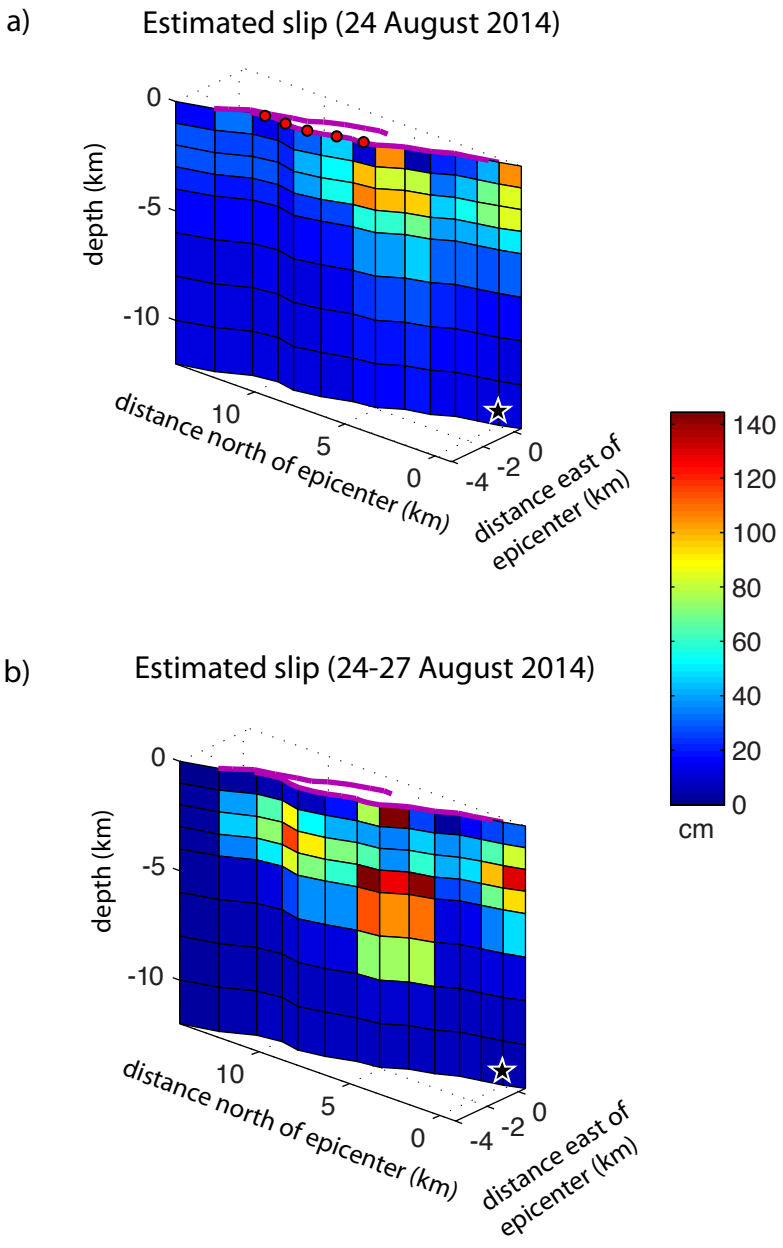
a)
Estimated slip (24 August 2014)
depth (km)
0
-5
-10
10
5
0
distance north of epicenter (km)
-4
-2
0
distance east of epicenter (km)
b)
Estimated slip (24-27 August 2014)
depth (km)
0
-5
-10
10
5
0
distance north of epicenter (km)
-4
-2
0
distance east of epicenter (km)
140
120
100
80
60
40
20
0
cm

Figure 10

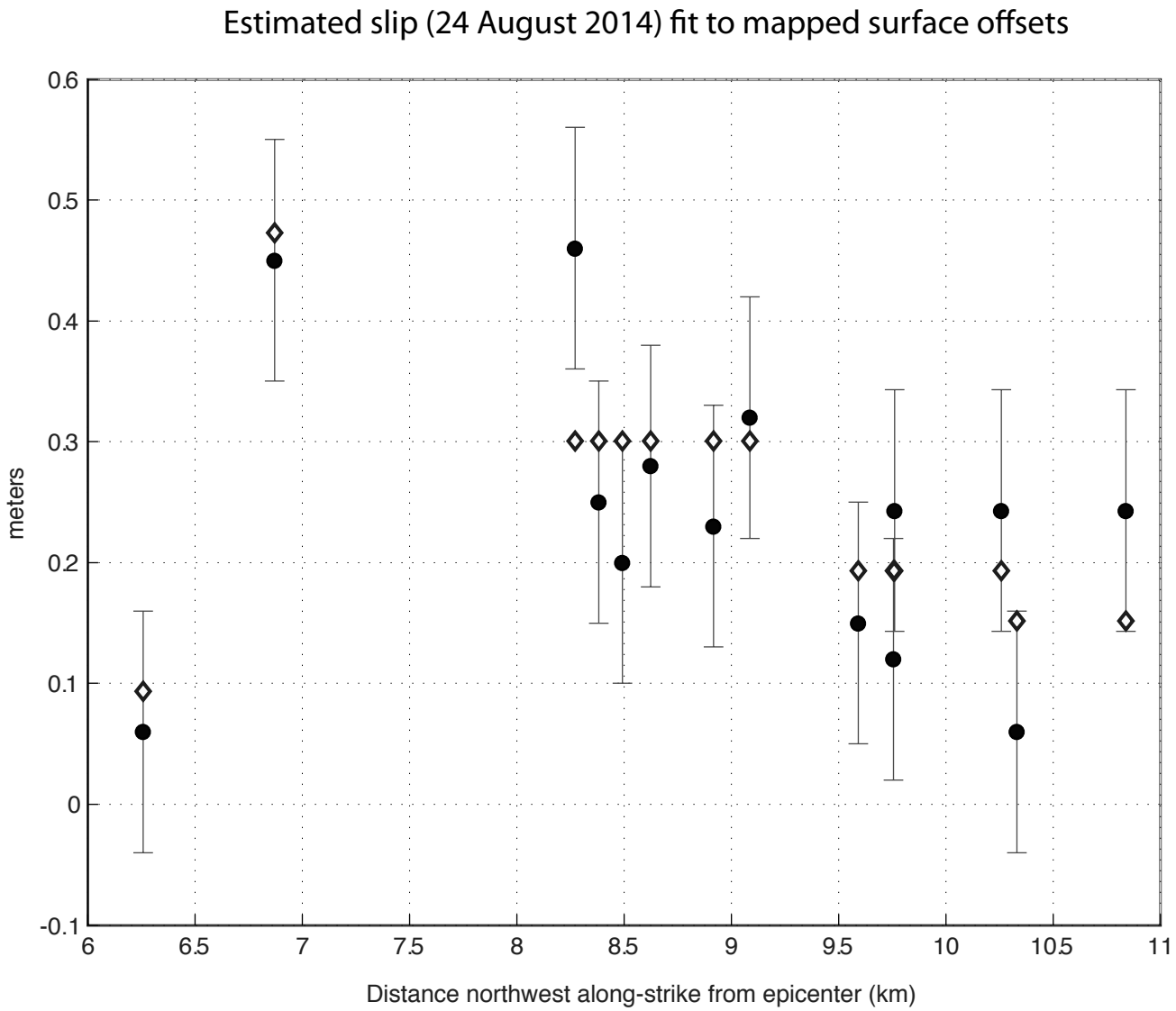
Estimated slip (24 August 2014) fit to mapped surface offsets
meters
0.6
0.5
0.4
0.3
0.2
0.1
0
-0.1
6
6.5
7
7.5
8
8.5
9
9.5
10
10.5
11
Distance northwest along-strike from epicenter (km)

Figure 11

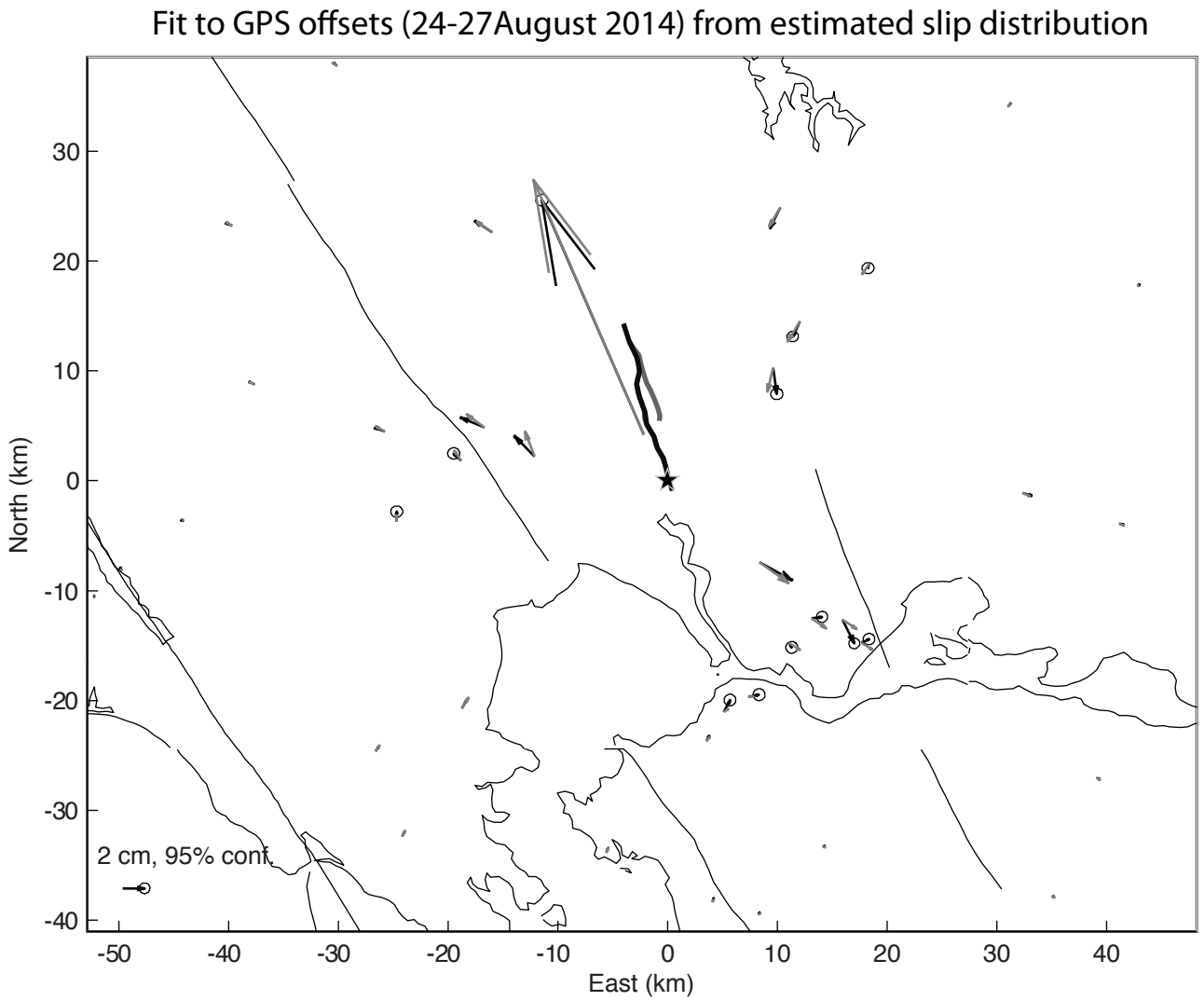
Fit to GPS offsets (24-27August 2014) from estimated slip distribution
North (km)
East (km)
2 cm, 95% conf.
30
20
10
0
-10
-20
-30
-40
-50
-40
-30
-20
-10
0
10
20
30
40

Figure 12
Click here to download high resolution image

Figure 13

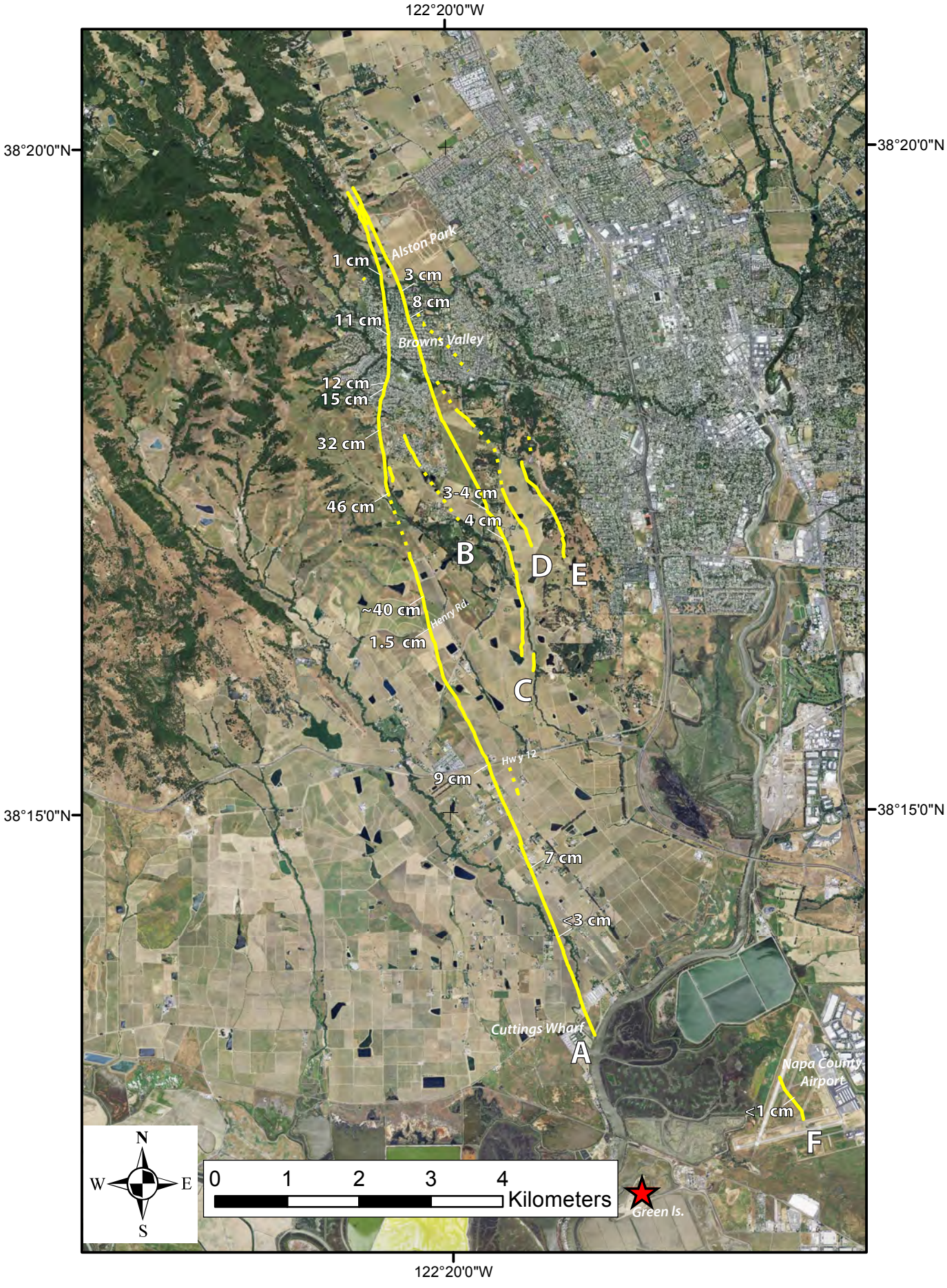
122°20'0"W
38°20'0"N
38°15'0"N
Alston Park
1 cm
3 cm
8 cm
11 cm
Browns Valley
12 cm
15 cm
32 cm
46 cm
3-4 cm
4 cm
B
D
E
~40 cm
Henry Rd.
1.5 cm
C
Hwy 12
9 cm
7 cm
<3 cm
Cuttings Wharf
A
Napa County Airport
<1 cm
F
N
W
E
S
0 1 2 3 4
Kilometers
Green Is.